MINISTRY OF SUPPLY

AERONAUTICAL RESEARCH COUNCIL
REPORTS AND MEMORANDA

Experiments on Two-dimensional Base

Flow at M = 2.4

By

L. FULLER and J. REID

LONDON : HER MAJESTY'S STATIONERY OFFICE

1958

TWELVE SHILLINGS NET

Experiments on Two-dimensional Base Flow at M = 2.4

By

L. Fuller and J. Reid

Communicated by the Principal Director of Scientific Research (Air),
Ministry of Supply

Summary.—This report gives an account of experiments carried out on a family of two-dimensional afterbodies to determine the effect of boat-tail angle and internal flow on the base pressure, the afterbody pressure, and the velocity distribution in the wake.

The afterbodies tested were of constant length with boat-tail angles of 0, $2\frac{1}{2}$, 5, $7\frac{1}{2}$ and 10 deg respectively. Each member of this series was mounted on a common model screwed to the upper surface of a flat plate placed at zero incidence in a uniform supersonic stream of Mach number 2·41. The inside of the model, which was hollow, was shaped in the form of a plenum chamber tapering towards the rear to a two-dimensional convergent nozzle with a parallel throat exhausting into the region behind the base. This nozzle was supplied with dry air at 20 deg C bled from the main tunnel supply.

Measurements were made of the afterbody pressure distribution, the base pressure, and the velocity distribution in the wake for each member of the family over a range of internal flow extending from no flow to $_tp_j/p_\infty = 11$. Further information on the base flow with the untapered afterbody was also provided by measurement of the effect of internal flow on the plate pressure distribution behind the base. In all cases these pressure measurements were supplemented by schlieren photography.

In the concluding sections of the report the results are analysed and discussed in detail both from the theoretical aspect and also with regard to their practical application.

1. *Introduction.*—The nature of the flow field behind a projectile in supersonic flight has long been of interest in the sphere of ballistics since a clear understanding of the processes governing flow breakaway at the base is essential for the prediction of the base drag, which forms an appreciable fraction of the total drag of the projectile.

For this reason the problem has been investigated extensively both experimentally and theoretically, but until recently only slight progress had been made towards its solution. From the theoretical aspect progress was, and to some extent still is, barred by the complexity of the viscous† mixing process in the wake which determines the angle of flow breakaway at the rear of the projectile and hence the pressure on the base. The experimental attack also was, of necessity, mainly confined to the measurement of deceleration and hence of total drag in a ballistics range, supplemented by instantaneous schlieren and shadowgraph photography.

---

† Throughout this report the term 'viscous' is used in a general sense to indicate the existence of shearing stress. It includes laminar mixing processes, in which the shearing stress is equal to the product of the coefficient of viscosity (μ) and the velocity gradient, and turbulent mixing processes.

Only indirect and comparative methods were available for isolating the base drag from the overall drag and the inadequate technique did not permit direct measurement of the base pressure or a detailed survey of the static pressure and velocity distribution in the wake.

Latterly, however, the advent of large supersonic wind tunnels and the application of rocket propulsion and telemetry to the free-flight technique has greatly extended the experimental data available on the base flow behind a projectile. The main features of the flow pattern have been brought to light, the variables affecting the base pressure isolated, and several[1,2] theories purporting to explain the observed results, advanced. Nevertheless, it must be emphasised that in each of these theories it has been found necessary to base the analysis on an over-simplified model of the actual flow field and consequently the range of application of the results obtained is strictly limited. A completely satisfactory theory based on a correct model of the flow field and in agreement with all the experimental evidence is still lacking.

In recent years the new field of application created by the rapid development of jet propelled supersonic aircraft and guided missiles has given fresh impetus to the study of base flow and research on the problem has been intensified. Further, since in many designs the propulsive jet is ejected from an axi-symmetric nozzle in the base of the missile, the scope of the enquiry has been extended to include the effect of this internal jet on the base pressure and the study of viscous mixing between two co-axial supersonic streams separated by an annular base.

The general problem is, therefore, complex, and although some work[3,4] on the effect of an internal jet has already been carried out it is clear that the need exists for a detailed and extensive study of the problem with the object of isolating the significant parameters, assessing their relative importance, and providing sufficient data for the construction of a comprehensive theory capable of predicting base pressure accurately over a wide range of conditions.

With this object in view, a new supersonic tunnel has been built which is to be devoted solely to research on afterbody and base flow. In this tunnel, interference effects due to model supports have been eliminated by the use of an annular axi-symmetric nozzle of which the after-body under test forms the central core. The facilities available allow variation in the stagnation pressure and temperature of the central jet over a fairly wide range and the equipment permits static pressure plotting over the surface of afterbody and base, pressure traversing of boundary layer and wake, direct drag measurement, and schlieren observation of the flow.

Before commencing an extensive set of tests on axi-symmetric models in this tunnel it was considered advisable first to investigate the analogous, but simpler, two-dimensional problem and accordingly a restricted programme was carried out on a simple family of two-dimensional models in a small existing two-dimensional tunnel. These preliminary tests form the subject of this report.

2. *General Discussion on Two-dimensional Base Flow.*—2.1. *The Case of a Rearward-facing Step in a Flat Plate.*—Before entering into an account of the experiment and the results obtained, it will be advantageous at this point briefly to review the main features of the flow pattern behind a sealed, two-dimensional base and to find by general reasoning the parameters which determine the base pressure. For this purpose it will be sufficient to examine a simple case, the flow in the vicinity of a rearward-facing step in a flat plate placed at zero incidence in a uniform supersonic stream[5]. An enlarged schlieren photograph of the flow field is shown in Fig. 1 and a schematic diagram of the flow pattern and pressure distribution along the plate in Fig. 2, to which we now refer.

It is clear that the flow will separate from the surface at the point B and the viscosity of the medium will cause momentum to be imparted to the air in the region behind the step BC. The boundary layer formed on the surface of the plate ahead of the step, of thickness AB, will therefore

2

spread downwards into the region behind the step and, of course, upwards into the free stream. In the figure, the upper and lower boundaries of this viscous flow or 'mixing' region are denoted by AG and BE respectively, the velocity at any point on AG being the free-stream velocity, and the velocity at any point on BE, zero. The line BF which separates the external flow from the entrained flow will be referred to henceforth as the 'flow dividing line'.

Now by continuity, since conditions are steady, BF must intersect the plate at some point P. The direction of flow of each streamline of the entrained air must therefore be reversed between F and P, so that BE also intersects the plate at P which is a stagnation point. Air trapped behind the step therefore circulates in a permanent vortex, being entrained by the mixing region between B and F and rejected between F and P. Between B and F the dominant process is one of viscous mixing so that the lines AG, BF and BE are straight and the static pressure in the region AGFEDCB is constant and equal to the base pressure (p_b). Between F and P, however, there must occur a pressure rise of sufficient magnitude to destroy the momentum of the entrained air. The line FP is therefore curved and a compression fan spreads from it into the free stream. Further, since BF is straight and the streamlines downstream of P are parallel to the plate the flow must be deflected towards the plate at B and an expansion fan radiates from this point. A weak shock wave of sufficient strength to force the boundary layer off the surface of the plate is located at the trailing edge of this expansion fan.

With regard to the pressure distribution we may assume that the flow above the line AGQH is substantially isentropic so that, since the net change in flow direction between B and P is zero, the uniform wake pressure (p_w) will be equal to the uniform pressure (p_∞) upstream of the step and the base pressure (p_b) will be less than either. The variation in pressure along the surface of the plate will therefore be of the form indicated in the figure.

2.2. *The Case of a Combined Afterbody and Base in the Absence of a Boundary Layer.*—Now for the limiting case in which the thickness of the boundary layer upstream of the step is zero we may, by a refinement of the reasoning outlined above, express p_b/p_∞ as a function of M_∞, and the velocity ratio (k) of the dividing streamline. The analysis, which follows the lines of two-dimensional jet mixing theory, is due to Kirk of the Royal Aircraft Establishment. It is valid under slightly more general geometrical conditions than the case previously considered and will be developed for a combined afterbody and base of the form shown in Fig. 3.

Referring to this figure we assume that:

(a)   the flow is everywhere adiabatic

(b)   there exists a point (F) on the flow dividing line such that this line is straight between A and F

(c)   within the region AGFE straight lines through A are lines of constant velocity

(d)   the static pressure in the region AGFE is constant

(e)   the flow is isentropic along the dividing line between F and P

(f)   the flow is isentropic along any streamline LM lying entirely above AGQH

(g)   downstream of PQ the flow is parallel to the plate and the static pressure uniform.

It follows immediately from assumptions (a), (b), (c), (d) and (e) that the velocity (u_c), Mach number (M_c) and static pressure (p_c) are constant along the dividing line between A and F and the total pressure ($_tp_c$) is constant between A and P.

Hence, since by assumption (d), $p_c = p_b$,

$$\frac{_tp_c}{p_b} = \left(1 + \frac{\gamma - 1}{2}M_c^2\right)^{\gamma/(\gamma - 1)}.$$

3

But since P is a stagnation point it follows from assumptions (f) and (g) that ${}_{\iota}p_c = p_\omega = p_\infty$, so that

$$\frac{p_\infty}{p_b} = \left(1 + \frac{\gamma-1}{2}M_c^2\right)^{\gamma/(\gamma-1)} \qquad \cdots \qquad \cdots \qquad \cdots \qquad (2.1)$$

Further, considering the streamline LM.

$$\frac{{}_{\iota}p_2}{p_2} = \left(1 + \frac{\gamma-1}{2}M_2^2\right)^{\gamma/(\gamma-1)}.$$

Hence, since by assumption (f), ${}_{\iota}p_\infty = {}_{\iota}p_2$ and, by assumption (d), $p_2 = p_b$, we have that

$$\frac{{}_{\iota}p_\infty}{p_b} = \left(1 + \frac{\gamma-1}{2}M_2^2\right)^{\gamma/(\gamma-1)}.$$

But

$$\frac{{}_{\iota}p_\infty}{p_\infty} = \left(1 + \frac{\gamma-1}{2}M_\infty^2\right)^{\gamma/(\gamma-1)},$$

so that

$$\frac{p_\infty}{p_b} = \left(\frac{1 + \frac{1}{2}(\gamma-1)M_2^2}{1 + \frac{1}{2}(\gamma-1)M_\infty^2}\right)^{\gamma/(\gamma-1)} \qquad \cdots \qquad \cdots \qquad \cdots \qquad (2.2)$$

If we now define k by the equation $k = u_c/u_2$ it follows by assumption (a) that

$$k^2 = \frac{M_c^2}{M_2^2}\left(\frac{1 + \frac{1}{2}(\gamma-1)M_2^2}{1 + \frac{1}{2}(\gamma-1)M_c^2}\right) \qquad \cdots \qquad \cdots \qquad \cdots \qquad (2.3)$$

and, eliminating M_c and M_2 from equations (2.1), (2.2) and (2.3), we find that:

$$\frac{p_b}{p_\infty} = \left[\frac{1 - k^2}{1 - \dfrac{k^2}{1 + \frac{1}{2}(\gamma-1)M_\infty^2}}\right]^{\gamma/(\gamma-1)}, \qquad \cdots \qquad \cdots \qquad \cdots \qquad (2.4)$$

which is the required relation between p_b/p_∞, M_∞ and k.

Now the quantity k depends solely on the process of viscous mixing occurring in the region AGFE. In general, therefore, we would expect that

$$k = f(M_2, Re_2), \qquad \cdots \qquad \cdots \qquad \cdots \qquad \cdots \qquad \cdots \qquad (2.5)$$

where $Re = u\rho/\mu$.

Moreover, elimination of p_b/p_∞ from equations (2.2) and (2.4) gives

$$M_\infty^2 = (1 - k^2)M_2^2 \qquad \cdots \qquad \cdots \qquad \cdots \qquad \cdots \qquad \cdots \qquad (2.6)$$

and it is easily shown that

$$\frac{Re_\infty}{Re_2} = g(M_2, M_\infty). \qquad \cdots \qquad \cdots \qquad \cdots \qquad \cdots \qquad \cdots \qquad (2.7)$$

4

Elimination of M_2 and Re_2 from equations (2.5), (2.6) and (2.7) gives

$$k = \zeta(M_\infty, Re_\infty) \qquad .. \qquad .. \qquad .. \qquad .. \qquad .. \qquad (2.8)$$

and, finally, eliminating k from equations (2.4) and (2.8) we obtain the relation

$$\frac{p_b}{p_\infty} = \phi(M_\infty, Re_\infty). \qquad .. \qquad .. \qquad .. \qquad .. \qquad .. \qquad (2.9)$$

We note that the boat-tail angle (ε) does not occur in equation (2.9). Basically this is, of course, due to the fact that M_2 is a unique function (given by the Prandtl-Meyer equation) of M_∞ and the flow deflection angle (ψ) (see Fig. 3). It is, in fact, of no consequence whether the total deflection ψ occurs entirely at A or successively at O and A.

On the same physical grounds we would therefore expect p_b/p_∞ to be independent of ε in the more general case when a boundary layer develops on the afterbody upstream of the base, although in these circumstances p_b/p_∞ will depend on the boundary-layer characteristics in addition to M_∞ and Re_∞.

The functional equation in the general case may therefore be written

$$\frac{p_b}{p_\infty} = \Phi\left[M_\infty, Re_\infty, \frac{\theta}{h}, \alpha\right], \qquad .. \qquad .. \qquad .. \qquad .. \qquad (2.10)$$

where θ is   momentum thickness of boundary layer

         h base height

         α a parameter depending on the state (laminar or turbulent) of the boundary layer and its velocity profile.

3. *Description of Model and Experimental Rig.*—All the tests were carried out on a half-model mounted on the upper surface of a flat plate placed at zero incidence in the working-section of a two-dimensional supersonic tunnel. This experimental arrangement effectively doubles the length of the working-section and also eliminates distortion of the flow field which might otherwise be produced by the model supports. It suffers from a potential disadvantage in that a boundary layer develops on the plate behind the base but it is considered that this has no significant effect on the results which should, therefore, be applicable to the case of a symmetrical model with the same profile.

A detailed drawing of the experimental arrangement is shown in Fig. 4 from which it will be seen that the inside of the model is hollow and consists of a plenum chamber tapering towards the rear to form a two-dimensional convergent nozzle with a parallel throat which exhausts into the region behind the base. This plenum chamber was supplied with dry air bled from the main-tunnel supply pipe by a duct, rectangular in section, passing through the bottom of the tunnel; the stagnation pressure in the throat of the internal nozzle being controlled by a valve and measured by two total-pressure probes placed symmetrically about the centre-line of the model, as shown. Great care was taken in the design and construction of the model to ensure that the whole of this internal air system was devoid of leaks as, under certain conditions, a small quantity of air bled into the base causes a marked increase in the base pressure.

A micrometer head which could be moved axially in a slot cut in the plate and vertically by means of a micrometer screw thread was used to determine the pressure distribution in the wake behind the base and in the boundary layer on the upper surface of the afterbody. Both total and static pressure surveys were made with this traversing gear using probes of $\frac{1}{2}$mm O.D.

and 1mm O.D. respectively, and the accuracy of location was approximately $\pm 0 \cdot 001$ in. over a rectangular region $1 \cdot 1$ in. long by $1 \cdot 6$ in. high bounded by the base on the left hand side and the plate beneath. All traversing was carried out in a vertical plane through the centre-line of the plate.

On completion of the main test programme it was decided that knowledge of the static-pressure distribution along the plate behind the base would be of assistance in the interpretation of the results. For this purpose the traverse gear was removed and a two-in. extension added to the original plate. Static-pressure holes spaced at $\frac{1}{4}$-in. intervals along the centre-line and extending from the base of the model to the trailing edge of the modified plate were then installed.

A family of five afterbodies, of constant length and with boat-tail angles of 0, $2\frac{1}{2}$, 5, $7\frac{1}{2}$ and 10 deg was selected for investigation. Fig. 5 shows the leading dimensions of each member of this family together with the location of the static-pressure points in the upper surface and base.

All the tests were carried out in a two-dimensional supersonic tunnel, $5\frac{1}{2}$ in. $\times$ $5\frac{1}{2}$ in. in cross-section, supplied with dry air at 20 deg C and atmospheric stagnation pressure. The model, which spanned the full width of the working-section, so that the flow was effectively two-dimensional, was mounted with its leading edge in the nozzle exit plane and $\frac{1}{2}$ in. above the surface of the lower liner. In this position, which was adopted after preliminary experiments, the tunnel could be started without choking, the boundary layer on the lower liner was deflected beneath the plate, the nose shock was attached, and by fitting a parallel extension to the upper liner a sufficient length of working-section free from disturbance was obtained. Alignment of the plate at zero incidence to the flow was facilitated by a three-point support system which could be adjusted while the tunnel was running.

Nozzle liners giving a Mach number $M = 2 \cdot 41$ ahead of the model were used throughout the experiment. With these liners the Mach number at the leading edge of the afterbody under test was $M_\infty = 2 \cdot 30$ and the corresponding Reynolds number $Re_\infty = 2 \cdot 7 \times 10^5$ per inch. The maximum attainable value of the ratio $_ip_j/p_\infty$ was $11 \cdot 0$.

A simple schlieren system was available for visual observation of the field of flow. Representative photographs taken with a horizontal knife edge and an exposure of 1/50 sec are shown in Figs. 1, 7 and 14.

4. *Details of the Experiment.*—4.1. *Nozzle Calibration.*—Prior to the commencement of afterbody tests the tunnel nozzle was calibrated to determine the free-stream Mach number ahead of the model. Total and static pressure traverses along a vertical line bisecting the leading edge of the model showed that the Mach-number distribution was substantially uniform and the Mach-number value $2 \cdot 41$.

A weak compression shock originating at the trailing edge of the upper liner passed downstream of the model mounting plate except during the measurement of the plate pressure distribution with afterbody No. 1 when, as mentioned in section 3, a two-inch extension was fitted to the standard plate. The effect of this weak shock on the plate pressure distribution is discussed in section 5.4.

4.2. *Main Test Programme.*—The main test programme may conveniently be divided under the following heads:

(*a*) *Afterbody Pressures.*—The static pressure distribution along the centre-line of the upper surface of each of the five afterbodies was measured at three conditions of internal flow ; namely, no internal flow, $_ip_j/p_\infty = 6 \cdot 5$ and $_ip_j/p_\infty = 11 \cdot 0$ (maximum flow).

6

(b) *Base Pressures.*—The base pressure was measured at a series of values of $_ip_j/p_\infty$ ranging from no internal flow to $_ip_j/p_\infty = 11\cdot0$. These measurements were made on afterbodies Nos. 1, 2, 3 and 4 only, as the base of afterbody No. 5 was of zero thickness.

(c) *Plate Pressures.*—In the case of afterbody No. 1 only, the variation in static pressure along the centre-line of the plate behind the base was determined over a range of internal flows extending from no flow to $_ip_j/p_\infty = 11\cdot0$.

(d) *Wake Traverses.*—Total and static pressure traverses were made along three vertical lines lying in the plane of symmetry of the model and spaced 0 in., 0·625 in. and 1·03 in. respectively downstream of the base. These traverses were carried out on all five afterbodies at three conditions of internal flow, *i.e.*, no flow, $_ip_j/p_\infty = 6\cdot5$ and $_ip_j/p_\infty = 11\cdot0$.

(e) *Boundary-Layer Traverses.*—The velocity profile in the boundary layer on the upper surface of afterbodies Nos. 1 and 5 was determined by total and static traverses along a vertical line in the plane of symmetry $\frac{1}{2}$ in. upstream of the base. Care was taken to ensure that the probes were aligned parallel to the surface in each case.

(f) *Schlieren Photographs.*—Schlieren photographs were taken to illustrate, firstly, the detailed effect of the internal jet on the flow behind afterbody No. 1 and, secondly, the field behind each afterbody at the three standard conditions of internal flow (No flow, $_ip_j/p_\infty = 6\cdot5$, and $_ip_j/p_\infty = 11\cdot0$).

4.3. *Additional Tests.*—In addition to the main test programme outlined above, two subsidiary experiments were carried out.

In the first of these an attempt was made to prove the existence of a region of reverse flow behind the base of afterbody No. 1 with no internal jet. For this purpose the wake was traversed vertically with a very small cotton tuft secured to a probe projecting through the plate and operated by the micrometer traversing gear. The existence of a region of reverse flow was clearly demonstrated but the boundaries of this region were ill-defined and could not be determined accurately.

Since the flow in the wake is, in general, inclined to the plate it was also necessary, in order to arrive at a correct interpretation of the wake traverse results, to investigate the effect of incidence on the pressure measured by static and total pressure probes. Calibration tests were therefore made with probes inclined at known angles to a uniform parallel supersonic stream.

5. *Discussion of Results.*—5.1. *Afterbody Pressures.*—The distribution of static pressure along the forebody and each of the five afterbodies under different conditions of internal flow is shown in Fig. 6. Referring to this figure it will be seen that, with afterbodies Nos. 1, 2 and 3, increasing the internal flow from zero to the maximum value obtainable ($_ip_j/p_\infty = 11\cdot0$) has no appreciable effect on the static pressure at any point on the surface. In the case of afterbody No. 4, however, the static pressure $\frac{1}{4}$ in. upstream of the base increases slightly with increase in $_ip_j/p_\infty$, and this effect is more pronounced with afterbody No. 5, for which the afterbody pressure at this point with full internal flow is about 80 per cent greater than the pressure with no internal flow.

Referring to the corresponding schlieren photographs in Fig. 7, no boundary-layer separation on the surface of the afterbody can be detected for afterbody No. 5 at $_ip_j/p_\infty = 6\cdot5$ and this is also true for afterbody No. 4 at all values of $_ip_j/p_\infty$ although the relevant schlieren photographs are, for the sake of brevity, not shown. Under these conditions, therefore, the observed increase in pressure must be caused by propagation of the pressure rise across the trailing-edge shock

7

upstream through the subsonic part of the boundary layer. On the other hand, the photograph for afterbody No. 5 at $p_j/p_\infty = 11\cdot0$ shows clearly that the boundary layer separates from the surface about $0\cdot3$ in. upstream of the base, producing a weak shock ahead of the main shock at the trailing edge, and consequently a marked rise in pressure on the surface of the afterbody.

Apart from these interference effects it is apparent from Fig. 6 that the pressure distribution along the afterbodies is fairly uniform and in agreement with that calculated by two-dimensional theory.

5.2. *Boundary-Layer Profiles.*—Fig. 8a shows the variation in Mach number across the boundary layer on the upper surface of afterbodies Nos. 1 and 5, $\frac{1}{2}$ in. upstream of the base. It is clear from the shape of these profiles that the boundary layer is turbulent in each case, as would be expected since the corresponding Reynolds number, based on model length, is approximately $2\cdot2 \times 10^6$. Inspection of Fig. 8a shows that the boundary-layer thickness (δ) is approximately $0\cdot10$ in. for afterbody No. 1 and $0\cdot15$ in. for afterbody No. 5, values which concur with the visual thickness measured from schlieren photographs. The displacement thickness (δ^*) and momentum thickness (θ), calculated from the velocity profiles by graphical integration, are tabulated in the figure. It will be seen that θ varies only slightly with ε so that the momentum thickness of the boundary layer on afterbodies Nos. 2, 3 and 4 may be calculated with sufficient accuracy, by linear interpolation.

The experimental points for both afterbodies when plotted in non-dimensional form, as in Fig. 8b, lie on the same curve and this curve is in fair agreement with the law $u/u_1 = (y/\delta)^{1/7}$, which is normally accepted for a turbulent boundary layer on a flat plate.

5.3. *The Effect of Boat-tail Angle on Base Pressure with No Internal Flow.*—The pressure ratio (p_b/p_∞) measured for afterbodies Nos. 1 to 4 with no internal flow is plotted against the boat-tail angle (ε) in Fig. 9a. In this connection a point arises which requires explanation. It will be appreciated that, since the height (H) of each member of the afterbody family is constant, both the boat-tail angle (ε) and the base height (h) alter in passing along the sequence and, if no further information were available, the observed variation in p_b/p_∞ could be attributed to the change in either ε or h or a combination of both variables. We have, however, indicated previously (section 2.2, equation (2.10)) that, for given values of M_∞, Re_∞ and the boundary-layer parameter (α), p_b/p_∞ is a unique function of θ/h and does not depend explicitly on ε, a result which has been experimentally confirmed. Since in the present tests M_∞, Re_∞ and α are constant, the observed variation in p_b/p_∞ with afterbody profile must, therefore, be attributed entirely to the corresponding change in θ/h. The relation between p_b/p_∞ and θ/h, which is plotted in Fig. 9b, is of considerable interest.

In the first place, for a fixed value of θ the size of the vortex behind the base will decrease with h so that the momentum transferred to this vortex will also decrease and p_b/p_∞ will consequently increase. Therefore p_b/p_∞ should increase with θ/h and the experimental results show that this is, in fact, the case. The linear dependence shown in Fig. 9b cannot, however, extend to large values of θ/h since it is clear that p_b/p_∞ tends to unity as θ/h tends to infinity.

Secondly, extrapolation of the experimental curve to $\theta/h = 0$ shows that in the absence of a boundary layer $p_b/p_\infty = 0\cdot281$ and by substituting in equation (2.4) of section 2.2 we find that the parameter $k = 0\cdot677$. That these values agree closely with the results of other experiments is shown by Fig. 10 in which $(p_b/p_\infty)_{\theta/h=0}$ and k are plotted against M_∞. Fig. 10 is also of interest with regard to equation (2.8) of section 2.2 since it shows that for constant Re_∞, k increases fairly rapidly with M_∞. The converse effect of Re_∞ on k at constant M_∞ is not known quantitatively but is believed to be small.

8

In Fig. 11 the afterbody pressure drag coefficient $(C_D)_A$, the base pressure drag coefficient $(C_D)_B$ and the overall pressure drag coefficient $(C_D)_T$ are plotted against ε and h/H. These coefficients are defined by the equations:

$$(C_D)_A = \frac{(p_\infty - p_1)(H - h)}{\tfrac{1}{2}\rho_\infty u_\infty^2 H} = \frac{2}{\gamma M_\infty^2}\left(1 - \frac{p_1}{p_\infty}\right)\left(1 - \frac{h}{H}\right),$$

$$(C_D)_B = \frac{(p_\infty - p_b)h}{\tfrac{1}{2}\rho_\infty u_\infty^2 H} = \frac{2}{\gamma M_\infty^2}\left(1 - \frac{p_b}{p_\infty}\right)\frac{h}{H},$$

$$(C_D)_T = (C_D)_A + (C_D)_B.$$

Fig. 11 shows that $(C_D)_T$ reaches a minimum value of $0\cdot144$ at a boat-tail angle of approximately 8 deg, and this optimum drag is 20 per cent less than the drag of a base without boat-tailing. Fig. 11 shows further that when the estimated skin-friction drag coefficient $(C_D)_S$ is taken into account, the overall drag coefficient $C_D = (C_D)_T + (C_D)_S$ also reaches a minimum value when $\varepsilon = 8$ deg and the percentage reduction in drag obtainable by boat-tailing is likewise the same.

5.4. *Plate Pressures—Afterbody No. 1 with No Internal Flow*.—The validity of the qualitative explanation, given in section 2.1, of the base flow behind a rearward-facing step in the presence of a boundary layer was confirmed by measurement of the static pressure distribution along the plate behind afterbody No. 1 with no internal flow. This distribution, together with the distribution of pressure across the base, is plotted in Fig. 12, and above the graph is shown a scale reproduction of the relevant schlieren photograph in Fig. 7.

It will be seen that from the base to a point $1\cdot5$ in. downstream the plate pressure is constant and approximately equal to the pressure across the base, which is also sensibly constant. This region corresponds to the upstream half of the vortex referred to in section 2.1, where the velocities are low and the vortex air is being entrained into the viscous flow region and accelerated by the external stream. In this region the dividing line is straight and the velocity along it is constant. The centre of the vortex is located approximately $1\cdot5$ in. downstream of the base.

Between $x = 1\cdot5$ in. and $x = 4\cdot5$ in. the plate pressure rises rapidly. This domain corresponds to the downstream half of the vortex where the entrained air, which has been accelerated to a high velocity, is first decelerated and then turned upstream by the pressure gradient. Over this length the dividing line is curved and a compression fan spreads into the free stream. At $x = 4\cdot5$ in. the dividing line touches the plate at a stagnation point which marks the downstream limit of the vortex.

Downstream of this stagnation point the plate pressure is constant and the streamlines are parallel to the plate. Assuming isentropic flow along any free streamline, p_p/p_∞ should be equal to unity in this region as the total change in flow direction is zero. The observed value of $p_p/p_\infty = 1\cdot07$ is attributed to a weak compression shock, originating at the trailing edge of the upper liner, which intersects the plate approximately 4 in. downstream of the base. This shock is visible in the schlieren photograph in Fig. 7 and its effect is marked by a slight increase, at $x = 4$ in., in the gradient of the plate pressure curve in Fig. 12.

5.5. *The Effect of Internal Flow on the Base Pressure—Afterbody No. 1*.—Having presented and discussed the results obtained without internal flow we turn now to the consideration of the effect on the base flow, and in particular on the base pressure, of an internal jet. This problem is, of course, more complicated than that of the sealed base since, in addition to the parameters already considered, p_b/p_∞ must also depend on the ratio $_1p_j/p_\infty$ and on the conditions in the upper boundary layer of the internal jet. Moreover, the theory advanced in sections

9

2.1 and 2.2 which served as a guide in the analysis of the previous results is no longer valid, although, as will be shown later, the same fundamental mechanism determines the base flow in the two cases. For these reasons we restrict the discussion initially to an analysis of the results obtained with afterbody No. 1 and consider the effect of $_ip_j/p_\infty$ on the base pressure and on the pressure distribution along the plate behind the base.

In Fig. 13 p_b/p_∞ is plotted against $_ip_j/p_\infty$ and the corresponding sequence of schlieren photographs is shown in Fig. 14. Referring to the graph in Fig. 13 it is apparent that as $_ip_j$ is increased the base pressure rises rapidly at first and p_b/p_∞ reaches a peak value of $0\cdot667$ when $_ip_j/p_\infty = 0\cdot750$. Further increase in $_ip_j$ results in a decrease in the base pressure until when $_ip_j/p_\infty = 2\cdot24$, p_b/p_∞ reaches a minimum value of $0\cdot385$, which is only slightly greater than the value obtained with a sealed base. Beyond this point the base pressure increases slowly but continuously with $_ip_j$ over the entire range of investigation. It will be shown that the basic physical mechanism which determines the shape of this curve may be divided naturally into two phases corresponding to the points 1 to 4 and 4 to 19 in the figure.

Now, apart from its inherent interest, Fig. 13 has an important practical application since it suggests that the introduction of a relatively small quantity of air into the base of the projectile would result in a substantial decrease in the base drag. In order to apply this effect to the best advantage, however, it is clearly essential that the underlying flow processes should be brought to light. The data presented in Figs. 13 and 14 proved insufficient for this purpose and further information was therefore sought from the effect of internal flow on the plate pressure distribution.

5.6. *The Effect of Internal Flow on the Plate Pressures—Afterbody No.* 1.—The first phase and the first part of the second phase of the effect of internal flow on the plate pressure distribution are shown in Figs. 15a and 15b in which p_p/p_∞ and $_ip_j/p_p$ respectively are plotted against the distance (x in.) downstream of the base. The range of internal flow covered by these curves extends from point (1) to point (12) in Fig. 13. Figs. 16a and 16b show similar graphs for the second part of the second phase corresponding to points (12) to (19) in Fig. 13. A sequence of schematic flow diagrams constructed by inference from these results and careful inspection of the schlieren photographs (Fig. 14) is shown in Fig. 17.

For the sake of clarity the analysis of this data will be divided into two sections corresponding to the two phases of the process.

Phase 1—(*Points* (1) *to* (4) *in Fig.* 13).—Referring first to Fig. 15a, the pressure distribution with no internal flow is given by the curve (1). This graph, which is, of course, identical with Fig. 12 has been discussed in detail in section 5.4. Fig. 17a illustrates the flow pattern.

Now, as $_ip_j$ is increased, part of the air entrained by the external flow is supplied by the internal jet and consequently the vortex decreases in size and moves downstream, and the momentum imparted by the external flow to the circulating air decreases. In consequence the pressure gradient necessary to reverse the direction of the vortex flow decreases, so that the angle of deflection of the external stream at the edge of the base becomes smaller and the base pressure therefore rises (*see* Fig. 15a, curves (2) and (3) and Fig. 17b). This trend continues until finally, at point (4), all the entrained air is supplied by the internal jet. When this condition is reached the quantity of recirculating air is reduced to zero and accordingly the pressure is approximately constant along the plate and the flow dividing line is straight (*see* Fig. 15a, curve (4) and Fig. 17c).

This sequence of events is confirmed by Fig. 15b which shows that for points (1), (2) and (3) the stagnation pressure of the internal jet is insufficient to surmount the pressure gradient along the plate and, in order to escape, the internal flow has to enter the mixing region and

acquire fresh momentum from the external stream. At point (4), however, $_i p_j/p_b = 1$ when $x = 5\cdot5$ in. so that the lower boundary of the mixing region intersects the trailing edge of the plate and all the entrained air is supplied by the internal jet.

Now although, as explained above, the original vortex becomes smaller and finally disappears during phase 1, it is clear that, as soon as the internal flow starts, a small vortex pair will be created in the region bounded by the internal and external flow and the base. Since the velocity of the internal jet is small during the first phase, the momentum imparted to this vortex pair is also small and has no significant effect on the plate pressure distribution. For this reason the existence of these vortices has been ignored in the preceding discussion. As, however, the exit velocity of the internal jet increases, the momentum transferred to this vortex pair by viscous mixing increases also and, in a manner precisely similar to that explained previously in section 5.4, a pressure gradient sufficient to reverse the direction of the vortex flow develops along the dividing lines AB and AC (Fig. 17c) so that the pressure at A (p_A) is greater than the base pressure at B and C. The dividing lines AB and AC are therefore curved. This effect first becomes measurable at point (4) and the pressure gradient referred to can be seen between $x = 0$ in. and $x = 1$ in. in Fig. 15a, curve (4). It will be noted that the exit velocity of the internal jet is still subsonic (*see* Fig. 15b, curve (4)).

Phase 2—(Points (4) *to* (19) *in Fig.* 13).—Beyond point (4) the velocity of the internal jet continues to increase with $_i p_j$ and reaches the sonic value between points (6) and (7) (*see* Fig. 15b). Thereafter an expansion fan develops with its origin at the point C (Figs. 17d to 17f) and the jet flow downstream of the base is supersonic. During the whole of phase 2, therefore, the velocity along the dividing line CA increases. The momentum of the vortex pair and consequently the pressure gradient along CA and BA therefore increase also, so that the base pressure decreases relative to the pressure at A.

Now since the pressure of both the internal and external streams must be the same at A, the flow direction and the pressure at this point can be calculated for given values of $_i p_j$ and p_∞ and it may readily be shown that, for constant p_∞, p_A increases with $_i p_j$.

During the first part of phase 2 (points (4) to (12) in Fig. 13) the decrease in p_b relative to p_A is greater than the increase in p_A relative to p_∞ with the result that p_b/p_∞ decreases. In the second part of phase 2, however, (points (12) to (19) in Fig. 13) the decrease in p_b relative to p_A is less than the increase in p_A relative to p_∞ so that p_b/p_∞ increases.

Typical schlieren photographs for phase 2 are shown in Fig. 14 and the corresponding flow patterns are illustrated by Figs. 17d to 17f. It will be seen that the pressure gradients along BA and CA give rise to compression fans spreading into the external and internal flows respectively. The effect of the internal compression fan on the plate pressure distribution may clearly be traced in curves (5) to (12) in Fig. 15a and (14) to (19) in Fig. 16a.

5.7. *The Effect of Boat-tail Angle and Internal Flow on the Base Pressure.*—In Fig. 18 p_b/p_∞ is plotted against $_i p_j/p_\infty$ treating the boat-tail angle (ε) as a parameter. It will be seen that the four curves are similar in shape, but for any given value of $_i p_j/p_\infty$ the ratio p_b/p_∞ increases with ε. Since, however, in passing from one member of the afterbody family to the next, both ε and the base height (h) alter, it is not possible to decide from the given data whether this effect is caused directly by the change in ε or whether, as shown in the case of no internal flow, it is an indirect effect caused by the change in θ/h. Further tests in which ε and h were varied independently would be required to decide this point.

Fig. 19 shows the corresponding family of curves for $(C_D)_T$, the overall pressure drag coefficient for the afterbody and base. In this connection $(C_D)_T$ is defined by the relation

$(C_D)_T = (C_D)_A + (C_D)_B$ where $(C_D)_A$, the afterbody pressure drag coefficient, and $(C_D)_B$, the base-pressure drag coefficient, are given by the equations:

$$(C_D)_A = \frac{(p_\infty - p_1)(H - h)}{\tfrac{1}{2}\rho_\infty u_\infty^2 H} = \frac{2}{\gamma M_\infty^2}\left(1 - \frac{p_1}{p_\infty}\right)\left(\frac{H - h}{H}\right),$$

$$(C_D)_B = \frac{(p_\infty - p_b)(h - h')}{\tfrac{1}{2}\rho_\infty u_\infty^2 H} = \frac{2}{\gamma M_\infty^2}\left(1 - \frac{p_b}{p_\infty}\right)\left(\frac{h - h'}{H}\right).$$

Fig. 19 is of considerable practical interest as it enables a comparison to be made of the relative effectiveness of base bleed and boat-tailing as methods for reducing the drag of a two-dimensional body, e.g., a supersonic wing with a blunt base. The figure shows that without boat-tailing (afterbody No. 1) the optimum drag coefficient with base bleed is equal to $0 \cdot 045$ compared with $0 \cdot 087$ without base bleed, a reduction of approximately 48 per cent. Moreover, since the minimum-drag point occurs when $_t p_j/p_\infty = 0 \cdot 75$ (i.e., less than unity), in a practical design the required bleed air could be drawn from the boundary layer on the external surface of the wing using a flush intake. It must, however, be emphasised that in any such practical arrangement the overall drag would be increased by the drag of the intake and associated ducting and, for this reason, the net reduction in drag would probably be less than the figure of 48 per cent quoted above. It is also clear from the shape of the graph that, in order to obtain the best results, the quantity of bleed air supplied to the base would have to be metered within narrow limits.

With regard to the effect of boat-tail angle, Fig. 19 shows that as ε is increased, the percentage reduction in drag obtainable by small quantities of bleed air decreases rapidly, and with afterbody No. 4 ($\varepsilon = 7 \cdot 5$ deg) the optimum drag coefficient is only 18 per cent less than the drag coefficient with no base bleed. This trend is largely due to the fact that, as ε increases, the base area decreases relative to the projected surface area of the afterbody. The optimum boat-tail angle may readily be determined from Fig. 19 by cross plotting $(C_D)_T$ against ε treating $_t p_j/p_\infty$ as a parameter. This optimum angle varies from approximately 4 deg when $_t p_j/p_\infty = 10$ to 8 deg with no internal flow, but at the latter condition $(C_D)_T$ is comparatively insensitive to variation in ε in the region of the optimum value.

5.8. *The Wake Traverses.*—In order to confirm the validity of the ideas presented in the preceding sections of this report concerning the nature of base flow, both with and without an internal jet, it was considered advisable, in addition to the indirect evidence afforded by measurement of the base and plate pressures, to carry out a detailed survey of the velocity distribution in the wake by means of pressure traverses.

A representative selection from the results obtained is shown in Figs. 20 to 26 inclusive, all the data for afterbodies Nos. 2 and 4, and the curves for afterbodies Nos. 3 and 5 at $_t p_j/p_\infty = 6 \cdot 5$ being omitted for the sake of brevity. The relevant schlieren photographs are included in Fig. 7.

Fig. 20 shows the Mach-number distribution behind afterbody No. 1 with no internal flow. In the schematic flow diagram at the head of this figure the lines B_1C_1 and B_3C_3 respectively mark the lower and upper boundaries of the mixing region and B_2C_2 is the flow dividing line.

Referring to the traverse at $x = 1 \cdot 03$ in. it will be seen that between the points C_0 and C_1 the measured flow velocity is zero. According to theory this region corresponds to the lower part of the vortex where the circulating air is moving slowly upstream, but the upstream velocity is apparently too small to produce any measurable difference between the total and static pressures. The existence of flow recirculation was, however, established by the tuft technique mentioned in section 4.3. In passing through the mixing region from C_1 to C_3 the Mach number

increases from zero to $M = 2 \cdot 95$ at C_3. Each layer of air in this zone is subjected to a downstream force on its upper surface and an upstream force on its lower surface due to viscosity. It will be appreciated that the air above C_2 comes from the external stream while below C_2 the flow consists of recirculating air. Between C_3 and C_4 the Mach number is constant but an abrupt increase in Mach number occurs between points C_4 and C_5 which mark respectively the lower and upper surfaces of a shock wave. The pressure gradient across this shock wave serves to separate the afterbody boundary layer from the base at the point O. Finally, in passing from C_5 to C_6 through the expansion fan originating at O, the Mach number decreases to the free-stream value.

The curve for $x = 0 \cdot 625$ in. is similar to that discussed above except that in this case the points B_3 and B_4 are coincident so that the region of uniform flow between the upper limit of the mixing region and the shock wave no longer exists.

It will be noted that the curves for $x = 0 \cdot 625$ in. and $x = 1 \cdot 03$ in. are consistent in that the Mach numbers at corresponding points (such as B_5, C_5, etc.) are equal and, moreover, the measured value of the free-stream Mach number at B_6 and C_6 is in agreement with the value calculated from the static pressure measured along the surface of the afterbody.

The Mach number distribution in the wake of afterbody No. 1 when $_tp_j/p_\infty = 6 \cdot 5$ is shown in Fig. 21 and will be considered with reference to the traverse at $x = 1 \cdot 06$ in. It will be seen that the expansion fan at the exit of the internal nozzle and its reflection from the plate cause the Mach number to increase between C_0 and C_1. In the compression fan marked by C_1 and C_2 the velocity decreases, thereafter remaining approximately constant until the lower boundary of the mixing region is reached at C_3. This mixing region extends from C_3 to C_5, the dividing line between the internal and external streams being marked by the point C_4. As would be expected, the velocity decreases in passing through the internal stream from C_3 to C_4 and then increases in traversing the external stream from C_4 to C_5. The velocity distribution in the mixing region between C_3 and C_5 is determined primarily by viscous forces. A zone of approximately uniform flow above C_5 is followed by an abrupt increase in the velocity caused by the shock wave between C_6 and C_7. Thereafter, in traversing the final expansion fan, the velocity decreases slightly to reach the free-stream value at C_8.

As a check on the consistency of the results it should be noted that in Fig. 21 the free-stream Mach number of the external flow is sensibly the same as that shown in Fig. 20. Moreover, comparison of Fig. 21 and Fig. 16b shows that at the points A_0B_0 and C_0 the Mach number calculated from the traverse results is in agreement with that calculated from the plate pressures.

Fig. 22 shows the velocity distribution behind afterbody No. 1 with $_tp_j/p_\infty = 11 \cdot 0$. It will be noted that the flow pattern in this case closely resembles the pattern for $_tp_j/p_\infty = 6 \cdot 5$ in Fig. 21 and the interpretation of the traverse results is similar in the two cases.

With regard to afterbody No. 3, the results with no internal flow are presented in Fig. 23 and the results for $_tp_j/p_\infty = 11 \cdot 0$ are shown in Fig. 24. Similar data for afterbody No. 5 will be found in Figs. 25 and 26 respectively. Detailed analysis of these results is unnecessary as the flow field behind afterbodies Nos. 3 and 5 bears a close resemblance to the field behind afterbody No. 1 with the same internal flow. It is, however, of interest to note, in connection with the traverse at $x = 0$ in. shown in Fig. 26 that the boundary layer separates from the surface of afterbody No. 5 when $_tp_j/p_\infty = 11 \cdot 0$ well upstream of the base. This separation, which is visible in the corresponding schlieren photograph in Fig. 7, causes a rise in pressure towards the rear of the afterbody (see section 5.1 and Fig. 6).

Before leaving the subject of the wake traverses it must be pointed out that considerable care is required in calculating the local Mach number from the observed pitot and static readings. The difficulties here are twofold.

In the first place it is known that in the neighbourhood of a strong disturbance, such as a shock wave, the static pressure measured by a probe differs from the true static pressure of the free stream (*i.e.*, the pressure existing at the same point when the probe is removed). The discrepancy is caused by propagation of the disturbance, both upstream and downstream, in the subsonic part of the boundary layer along the surface of the probe. For this reason, in reducing the present results, no use has been made of static pressure readings taken within $0 \cdot 05$ in. of a shock wave or strong compression fan.

In the second place errors may be caused in both the static and pitot pressure readings, particularly the former, owing to the fact that, in general the wake flow is inclined to the plate and hence to the axis of the traverse probe. A subsidiary investigation showed that an error of 1 per cent corresponds to an angle of incidence of 6 deg with the static-pressure probe and 16 deg with the total-pressure probe and accordingly no use has been made of static- and total-pressure measurements taken when the angle of incidence exceeded 6 deg and 16 deg respectively.

Two different methods of calculation were adopted depending on whether internal flow was present or not. In the case of no internal flow (*see*, e.g., the traverse at $x = 1 \cdot 03$ in. in Fig. 20), the assumption was made that the static pressure in the mixing region between C_1 and C_3, and in the free stream between C_3 and C_4 was constant and equal to the static pressure (p) in the zone $C_0 C_1$ where the flow velocity was zero and the observed readings therefore correct (The validity of this assumption was verified for the traverse at $x = 1 \cdot 03$ in. with afterbody No. 1 using a static probe parallel to the direction of flow). As the flow angle did not exceed 16 deg between C_0 and C_4 the measured pitot pressure ($_tp'$) was correct to within 1 per cent in this region and the local Mach number (M) was calculated from the ratio $_tp'/p$. In the expansion fan between C_5 and C_6 the measured static pressures were ignored and M computed from the ratio $_tp'/_tp_\infty$ assuming isentropic flow upstream of the line $C_5 C_6$.

The procedure with internal flow may be explained with reference to the traverse at $x = 1 \cdot 06$ in. shown in Fig. 21. In the internal jet between C_0 and C_1, M was determined from the ratio $_tp'/_tp_j$ on the assumption that no loss of total pressure occurred between the throat of the internal nozzle and the traverse plane. Between C_2 and C_6, where the angle of incidence was, in general, not more than 6 deg, the observed values of both $_tp'$ and p were accurate to within 1 per cent and consequently the ratio $_tp'/p$ served to determine M. Above C_7 the static pressures were ignored and M calculated from $_tp'/_tp_\infty$ as for the case of no internal flow.

6. *Conclusions.*—The more important conclusions drawn from the results presented and discussed in the preceding sections of this report may be summarised thus:

(*a*) *Base Flow with No Internal Jet.*—(i) In this case the external flow separates from the surface at the edge of the base and the boundary layer formed on the surface of the afterbody spreads upwards into the free stream and downwards into the space behind the base to form a viscous flow or 'mixing' region. Air entrained and accelerated by the external flow in this mixing region is subsequently slowed down and recirculated in a region of compression which occurs where the external stream reattaches itself to the plate. The air trapped behind the base circulates, therefore, in a permanent vortex. In general, the velocity and pressure distribution in the wake and, in particular, the base pressure, are determined by a balance between viscous forces, which tend to increase the kinetic energy of the vortex, and inertia forces which tend to decrease it.

(ii) The tests, which were carried out at $M_\infty = 2 \cdot 30$ and $Re_\infty = 2 \cdot 7 \times 10^5$ per inch, with a turbulent boundary layer, show that, within the range of investigation, p_b/p_∞ increases linearly with θ/h (Fig. 9b). Extrapolation of the experimental curve to $\theta/h = 0$ gives $p_b/p_\infty = 0 \cdot 281$ in the absence of a boundary layer and the corresponding value of k obtained by substitution in equation (2.4) is $k = 0 \cdot 677$. These values correlate closely with the results of previous tests carried out at different Mach numbers but approximately the same Reynolds number (Fig. 10).

14

(iii) The overall pressure drag coefficient $(C_D)_T$ for the combined afterbody and base reaches a minimum value of $0 \cdot 144$ at a boat-tail angle of approximately 8 deg (Fig. 11). This optimum drag is 20 per cent less than the drag of a base without boat-tailing.

(b) *Base Flow with Internal Jet.*—(i) The effect of internal flow on the base pressure falls naturally into two phases (Fig. 13). In the first phase, as $_ip_j/p_\infty$ is increased, part of the air entrained by the external flow is supplied by the internal jet and consequently the vortex decreases in size and p_b/p_∞ increases. This trend continues until, at the end of the first phase, the quantity of recirculating air is reduced to zero and the internal jet is fully established, *i.e.*, the internal flow can just escape without entering the mixing region. At this point p_b/p_∞ is a maximum, but the exit velocity of the internal jet is still subsonic.

Further increase in $_ip_j/p_\infty$ (phase 2), results first in a drop in p_b/p_∞ followed finally by a steady rise. During this phase the pressure (p_A) at the junction of the internal and external streams increases with $_ip_j$ but, owing to the formation of a vortex pair between the base and the internal and external streams, p_b decreases relative to p_A and the resultant influence of $_ip_j/p_\infty$ on p_b/p_∞ depends on the relative magnitude of these two effects.

(ii) The graph of $(C_D)_T$ plotted against $_ip_j/p_\infty$ and ε (Fig. 19) shows that without boat-tailing the optimum drag coefficient with base bleed is equal to $0 \cdot 045$ compared with $0 \cdot 087$ without base bleed, a reduction of 48 per cent. As ε is increased, however, the percentage reduction in drag obtainable by base bleed decreases, being only 18 per cent when $\varepsilon = 7 \cdot 5$ deg. The optimum boat-tail angle varies from approximately 4 deg when $_ip_j/p_\infty = 10$ to 8 deg with no internal flow. In practice, the net reduction in drag obtainable by base bleed would probably be appreciably less than the figures quoted above on account of the drag of the bleed air intake and ducting.

(iii) Within the range of internal flow tested $(_ip_j/p_\infty \leqslant 11 \cdot 0)$ the internal jet has no effect on the afterbody pressure distribution provided that the boat-tail angle (ε) is not greater than 5 deg. When ε is more than this the boundary layer separates from the afterbody slightly upstream of the base at large internal flows and the afterbody pressure near the trailing edge increases. When $\varepsilon = 7 \cdot 5$ deg the pressure $\frac{1}{4}$ in. upstream of the base when $_ip_j/p_\infty = 11 \cdot 0$ is some 10 per cent greater than the pressure with no internal flow and the corresponding figure for $\varepsilon = 10$ deg is 80 per cent (Fig. 6).

LIST OF SYMBOLS

(1) *Dimensions of Model (see* Fig. 5)

L	Overall length of model
H	Maximum height of model
l	Length of afterbody
h	Base height
h'	Height of internal jet
ε	Boat-tail angle

(2) *Flow Parameters*

p	Static pressure
M	Mach number
ρ	Density
u	Velocity
μ	Viscosity
Re	Reynolds number per unit length
	$= \dfrac{u\rho}{\mu}$

The flow field is divided into reference zones and the parameters in each zone indicated by a suffix as shown in Fig. 3. The suffix $_j$ refers to the internal jet.

Quantities referred to stagnation conditions are prefixed by the letter $_t$.

In the wake traverses, primed symbols refer to conditions behind a normal shock wave at the point in question.

(3) *Boundary-Layer Parameters*

δ	Thickness of the boundary layer
δ^*	Displacement thickness of the boundary layer
	$= \displaystyle\int_0^{\delta}\left(1 - \frac{\rho u}{\rho_1 u_1}\right)dy$
θ	Momentum thickness of the boundary layer
	$= \displaystyle\int_0^{\delta}\frac{\rho u}{\rho_1 u_1}\left(1 - \frac{u}{u_1}\right)dy$
α	A parameter depending on the state (laminar or turbulent) of the boundary layer and its velocity profile (*see* section 2.2)

REFERENCES

No.	Author	Title, etc.
1	D. R. Chapman	An analysis of base pressure at supersonic velocities and comparison with experiment. N.A.C.A. Report 1051. 1951. N.A.C.A. Tech. Note 2137. July, 1950.
2	W. F. Cope	The effect of Reynolds number on the base pressure of projectiles. N.P.L. Report Eng. Div. 63/44. Jan., 1945.
3	E. M. Cortright, Jr. and A. H. Schroeder	Preliminary investigation of effectiveness of base bleed in reducing drag of blunt-base bodies in supersonic stream. N.A.C.A. Res. Mem. E.51.A.26. March, 1951. N.A.C.A./T.I.B./2656.
4	E. S. Love	Aerodynamic investigation of a parabolic body of revolution at $M = 1.92$ and some effects of an annular jet exhausting from the base. N.A.C.A. Res. Mem. L.9.K09. Feb., 1950. N.A.C.A./T.I.B./2525.
5	D. Beastall and H. Eggink	Some experiments on breakaway in supersonic flow (Part II). R.A.E. Tech. Note Aero. 2061. June, 1950.
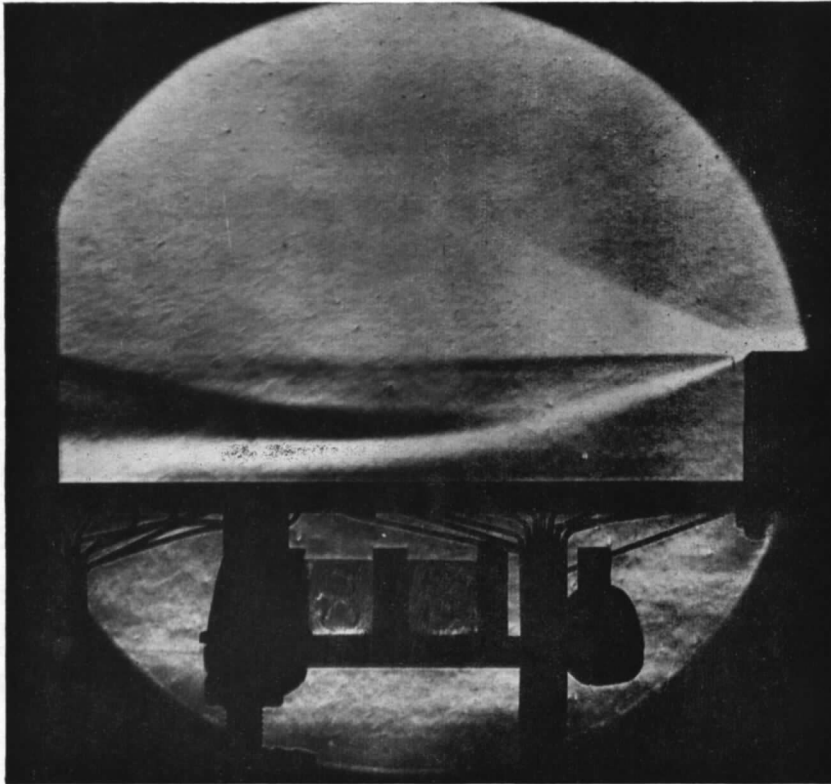
FIG. 1. Schlieren photograph of the flow behind a rearward-facing step.
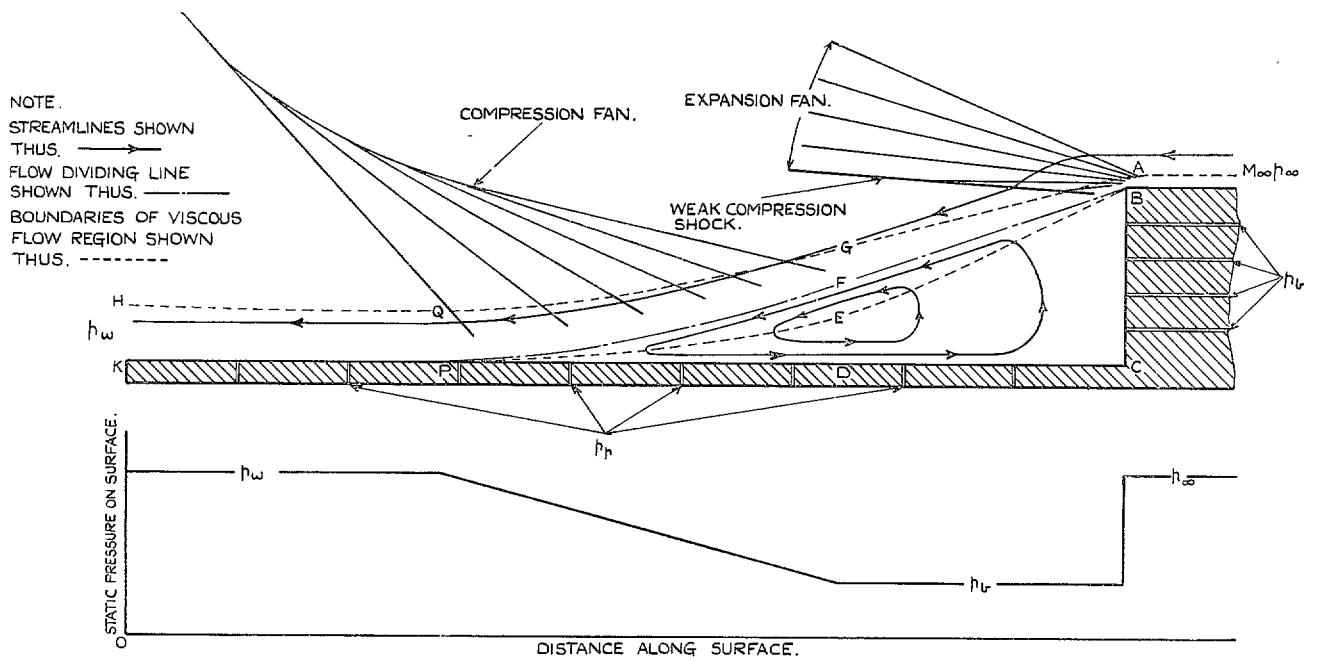
Fig. 2.   Schematic diagram showing flow pattern and surface pressure distribution behind rearward-facing step with boundary layer.
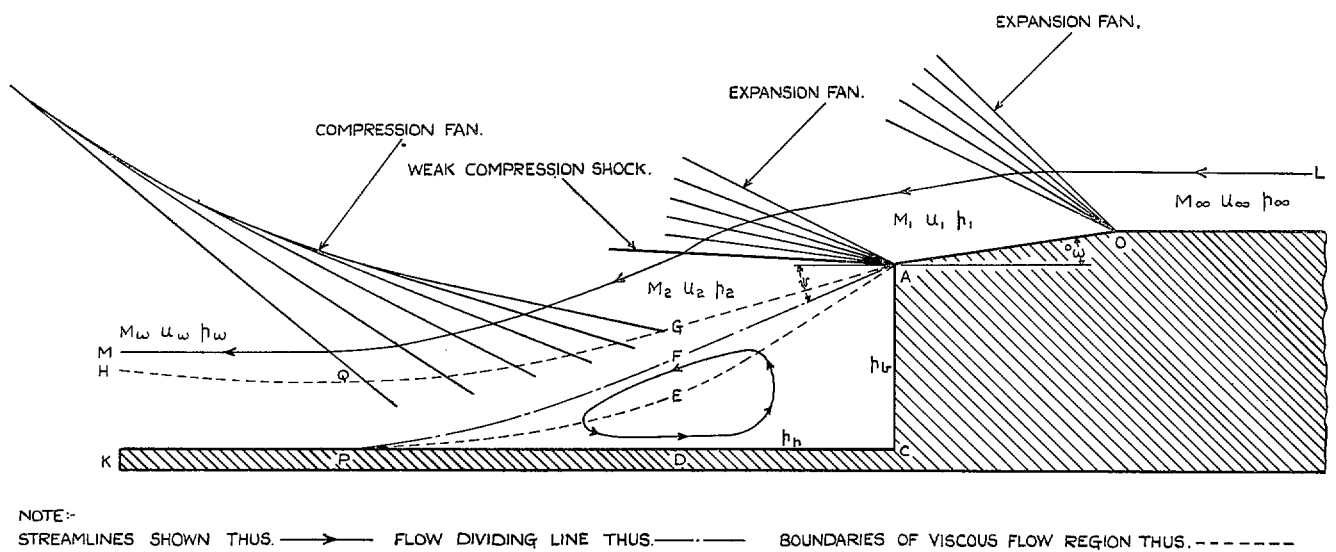
Fig. 3.   Schematic diagram showing flow pattern behind two-dimensional afterbody and base in absence of boundary layer.
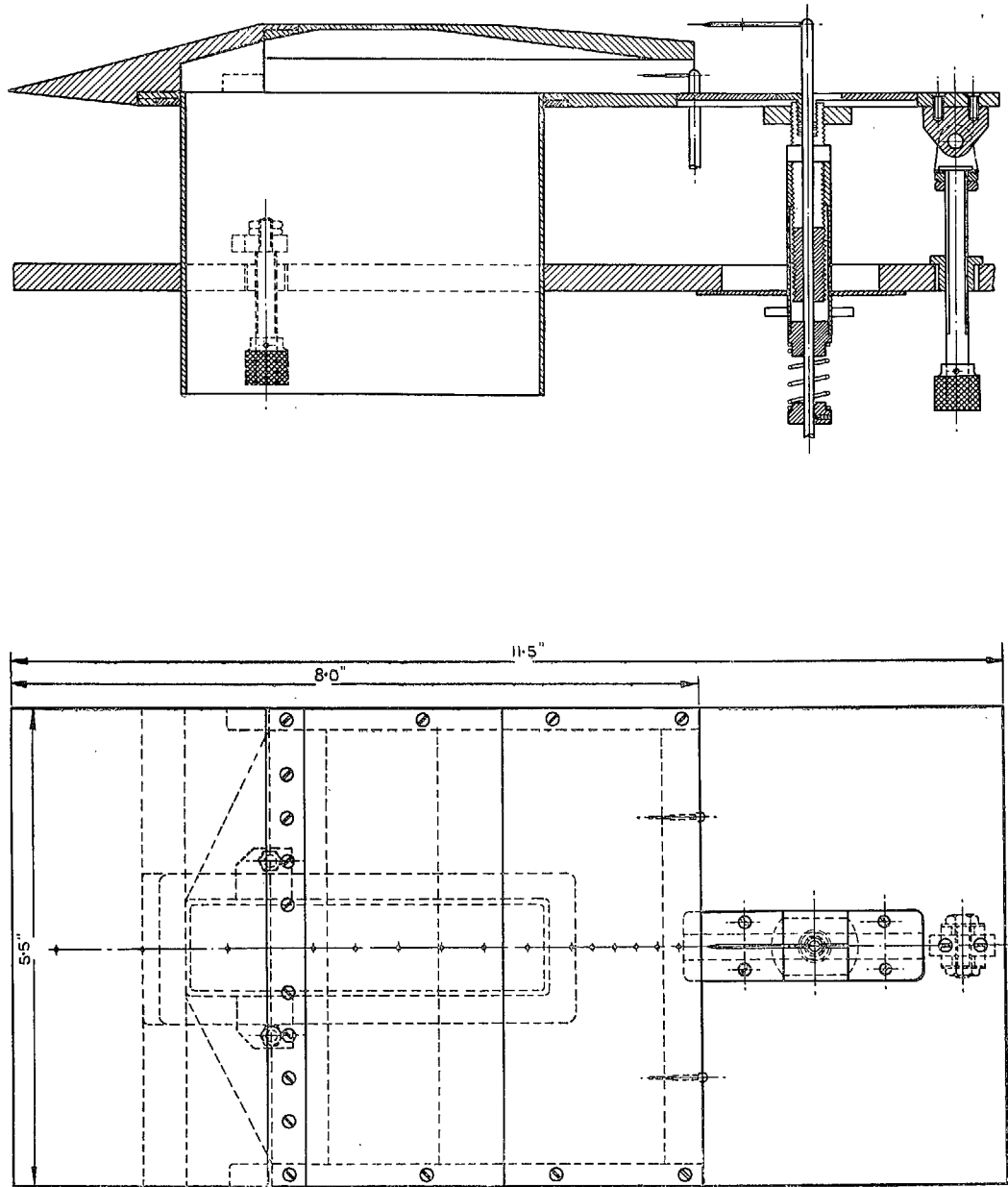
18

FIG. 4. General arrangement drawing—Two-dimensional model for afterbody tests.
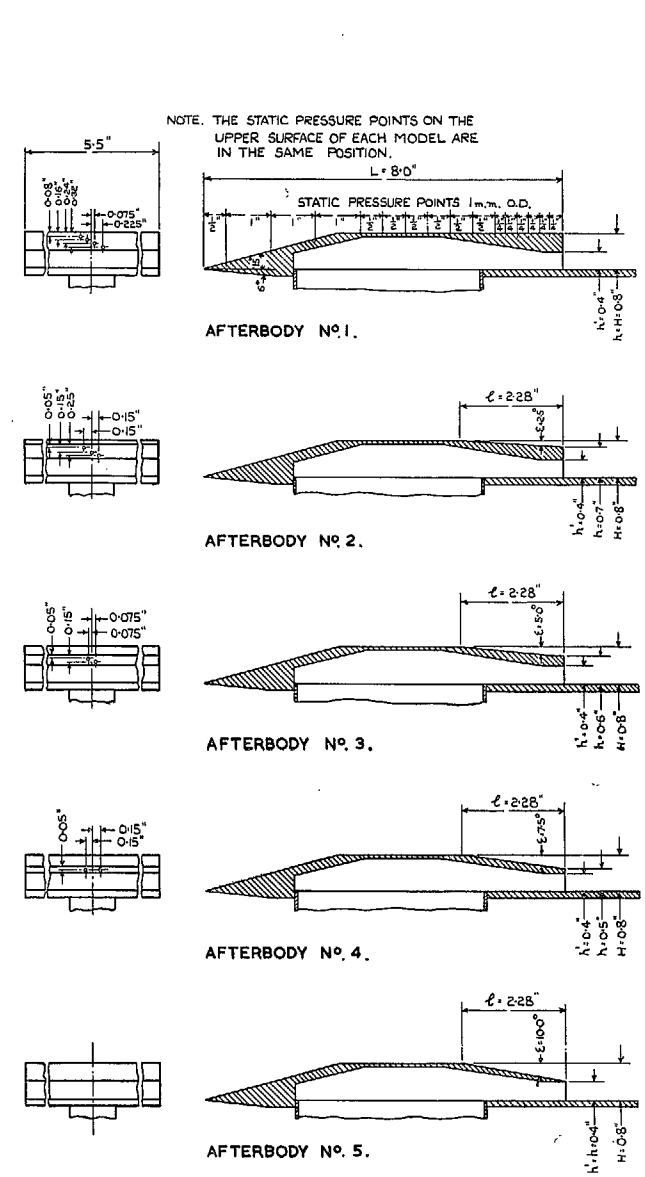
NOTE. THE STATIC PRESSURE POINTS ON THE UPPER SURFACE OF EACH MODEL ARE IN THE SAME POSITION.

AFTERBODY N⁰. 1.

AFTERBODY N⁰. 2.

AFTERBODY N⁰. 3.

AFTERBODY N⁰. 4.

AFTERBODY N⁰. 5.

FIG. 5. Two-dimensional afterbodies Nos. 1 to 5—Leading dimensions and position of static pressure points.
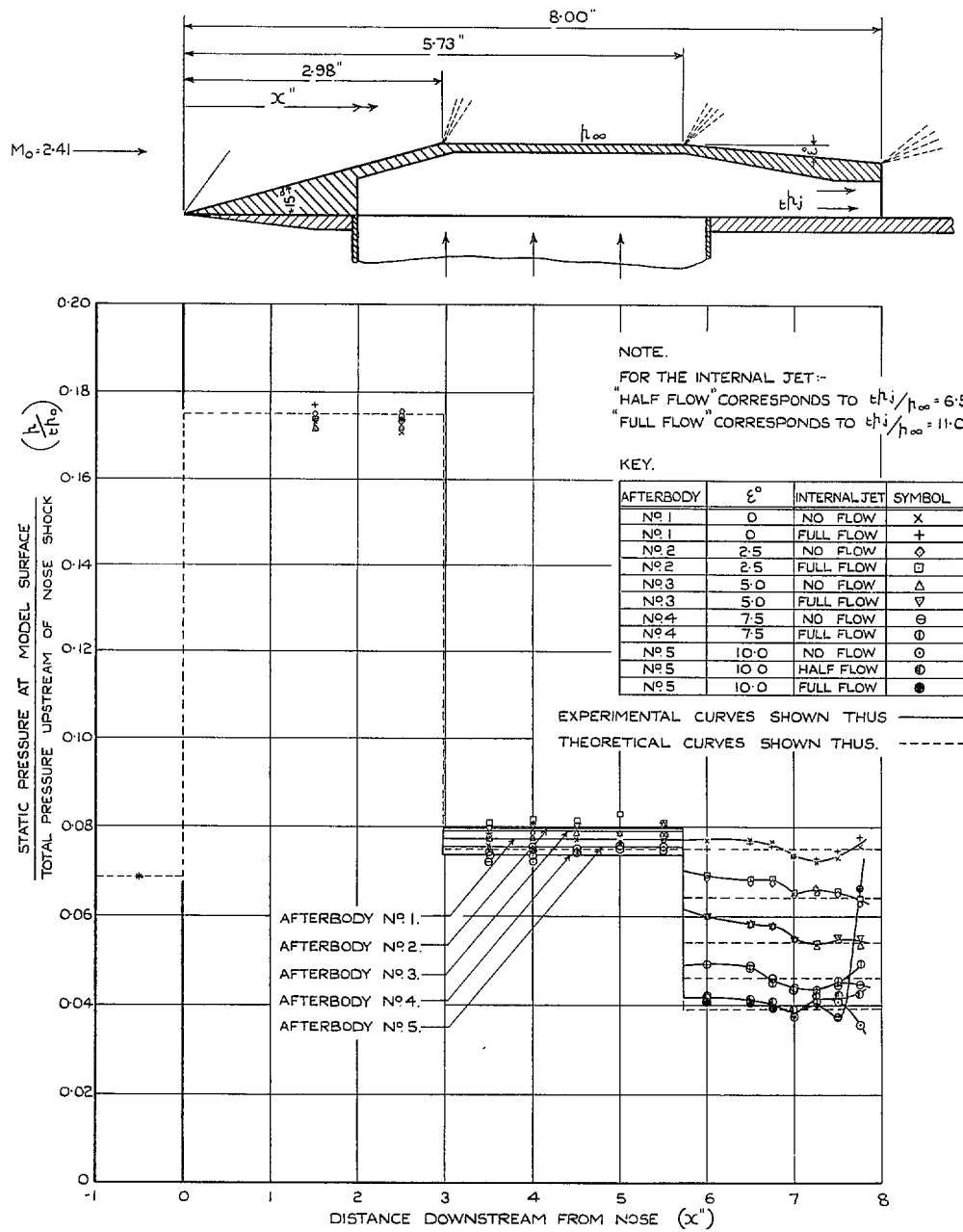
FIG. 6. Effect of boat-tail angle and internal jet on static pressure distribution along surface of model.

Top diagram labels:

8·00"

5·73"

2·98"

x''

$M_o = 2·41$

h_∞

$\frac{t^h j}{}$

Graph axis labels:

Y-axis (left): STATIC PRESSURE AT MODEL SURFACE / TOTAL PRESSURE UPSTREAM OF NOSE SHOCK $\left(\frac{h}{t h_o}\right)$

Y-axis values: 0·20, 0·18, 0·16, 0·14, 0·12, 0·10, 0·08, 0·06, 0·04, 0·02, 0

X-axis: DISTANCE DOWNSTREAM FROM NOSE (x'')

X-axis values: -1, 0, 1, 2, 3, 4, 5, 6, 7, 8

In-graph labels:

AFTERBODY Nº 1.
AFTERBODY Nº 2.
AFTERBODY Nº 3.
AFTERBODY Nº 4.
AFTERBODY Nº 5.

Note block:

NOTE.

FOR THE INTERNAL JET :-
"HALF FLOW" CORRESPONDS TO $t^h j / h_\infty = 6·5$.
"FULL FLOW" CORRESPONDS TO $t^h j / h_\infty = 11·0$.

KEY.

AFTERBODY	ξ^o	INTERNAL JET	SYMBOL
Nº 1	O	NO FLOW	X
Nº 1	O	FULL FLOW	+
Nº 2	2·5	NO FLOW	◇
Nº 2	2·5	FULL FLOW	▱
Nº 3	5·0	NO FLOW	△
Nº 3	5·0	FULL FLOW	▽
Nº 4	7·5	NO FLOW	⊖
Nº 4	7·5	FULL FLOW	⊕
Nº 5	10·0	NO FLOW	⊙
Nº 5	10·0	HALF FLOW	◐
Nº 5	10·0	FULL FLOW	●

EXPERIMENTAL CURVES SHOWN THUS ———

THEORETICAL CURVES SHOWN THUS. ------

20

Afterbody No. 1.   No internal flow.

Afterbody No. 3.   No internal flow.

Afterbody No. 5.   No internal flow.

Afterbody No. 1. $\dfrac{tp_j}{p_\infty} = 6.5.$

Afterbody No. 3. $\dfrac{tp_j}{p_\infty} = 6.5.$

Afterbody No. 5. $\dfrac{tp_j}{p_\infty} = 6.5.$

Afterbody No. 1. $\dfrac{tp_j}{p_\infty} = 11.0.$

Afterbody No. 3. $\dfrac{tp_j}{p_\infty} = 11.0$

Afterbody No. 5. $\dfrac{tp_j}{p_\infty} = 11.0.$

FIG. 7.   Schlieren photographs showing effect of boat-tail angle and internal jet on base flow.

21
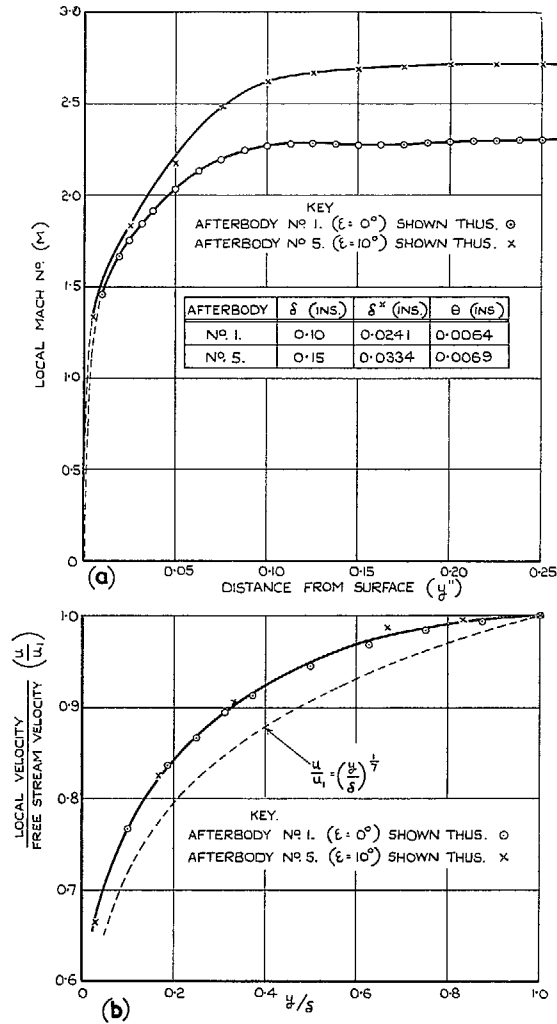
FIGS. 8a and 8b. Turbulent boundary layer—
Velocity profiles ($M_\infty = 2 \cdot 30$. $Re_\infty = 2 \cdot 7 \times 10^5$
per inch).
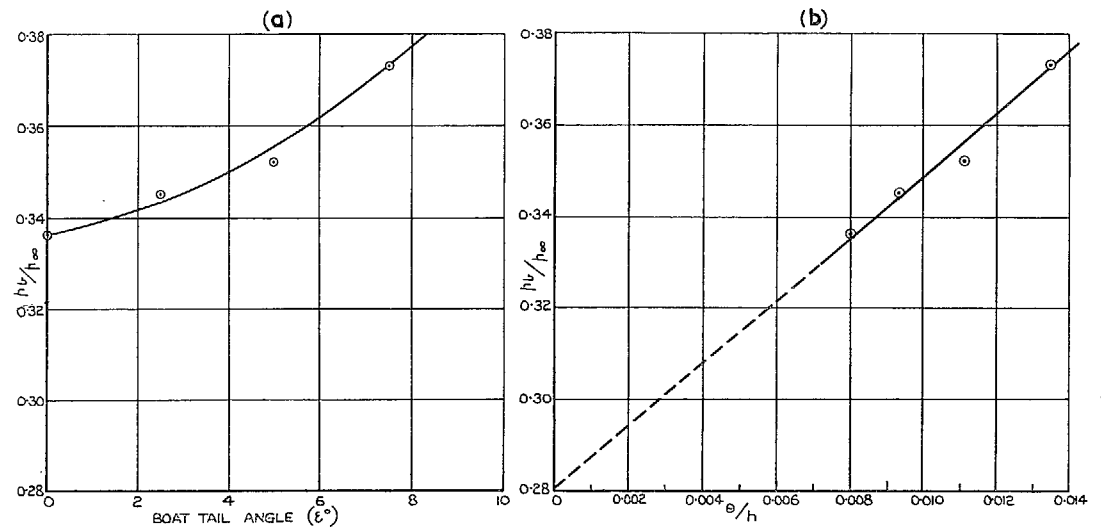
FIGS. 9a and 9b. Effect of boat-tail angle ($\varepsilon°$) and the ratio $\dfrac{\text{momentum thickness of boundary layer}}{\text{base height}}$
(θ/h) on base pressure ($M_\infty = 2 \cdot 30$. $Re_\infty = 2 \cdot 7 \times 10^5$ per inch. Turbulent boundary
layer. No internal flow).

KEY.

ALL POINTS ARE DERIVED FROM EXPERIMENTAL CURVES OF (h_{b}/h_{∞}) AGAINST (θ/h) AT CONSTANT M_{∞} AND Re_{∞} BY EXTRAPOLATION TO $\theta/h = 0$.

⊙ DENOTES PRESENT TESTS.
▢ DENOTES TESTS REPORTED IN REF. 5.

SEE SECTION 2·2 FOR DEFINITION OF (K)

K = 0·643

K = 0·659

K = 0·677

K = 0·713

M_{∞}

OVERALL DRAG (PRESSURE + ESTIMATED SKIN FRICTION)

$\ell = 2·27''$
$H = 0·80''$

OVERALL PRESSURE DRAG

BASE PRESSURE DRAG.

AFTERBODY PRESSURE DRAG.

h/H
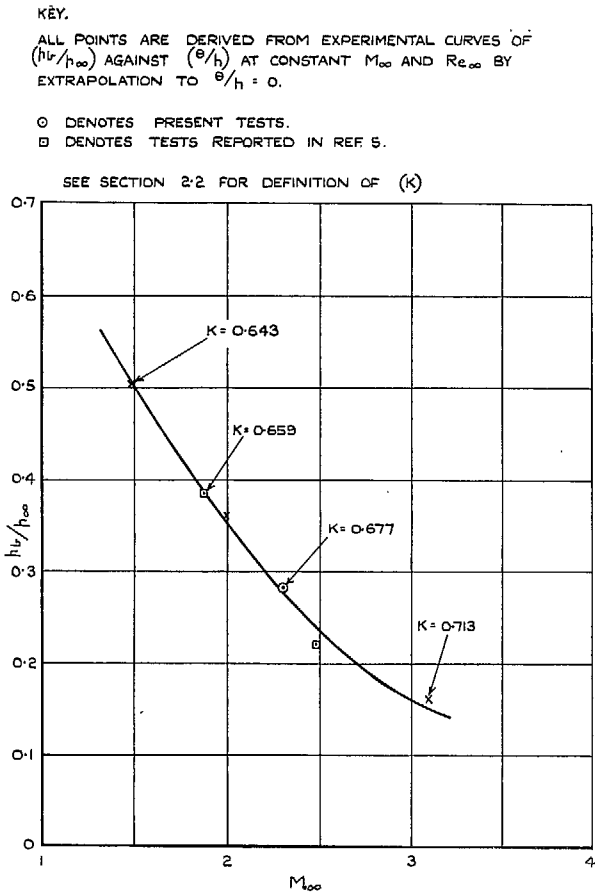
Fig. 10. Effect of Mach number (M_{∞}) on base pressure (p_{b}/p_{∞}) (No boundary layer $(\theta/h = 0)$. No internal flow. $Re_{\infty} = 2·7 \times 10^{5}$ per inch).
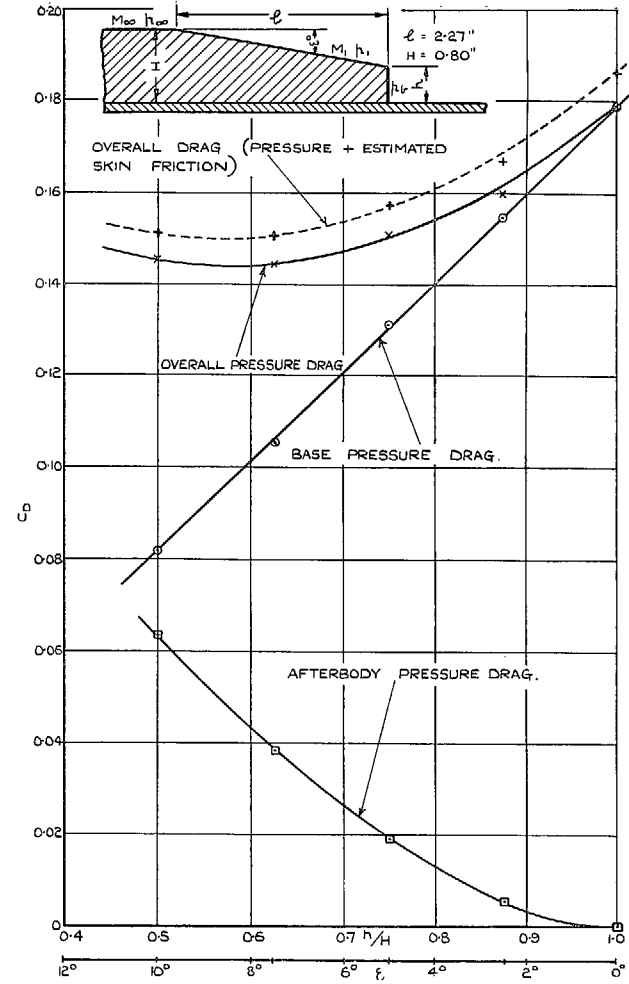
Fig. 11. Effect of boat-tail angle on drag coefficients $(M_{\infty} = 2·30.\quad Re_{\infty} = 2·7 \times 10^{5}$ per inch. Turbulent boundary layer. No internal flow).
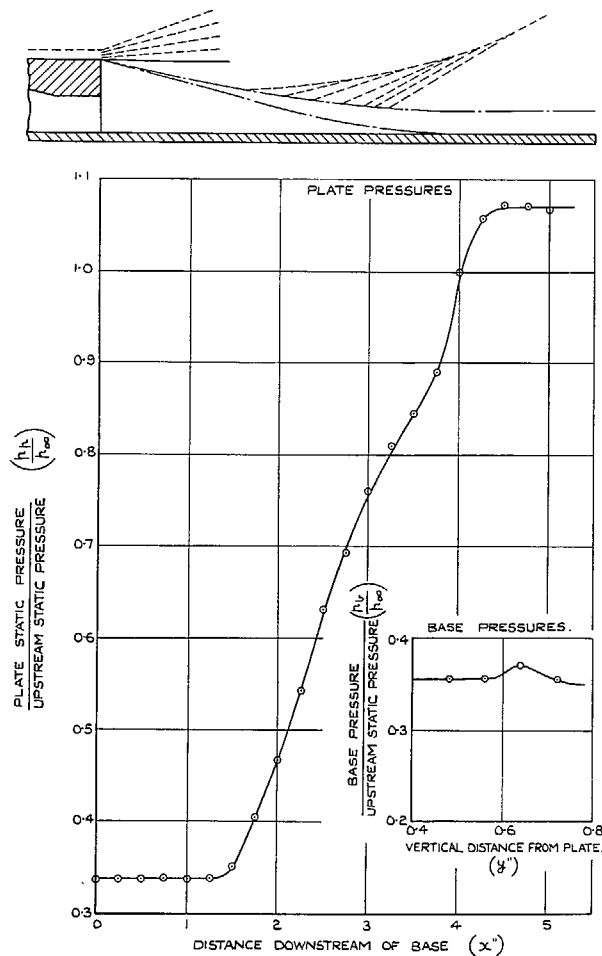
FIG. 12. Static-pressure distribution across base and along plate—Afterbody No. 1 (No internal flow. Turbulent boundary layer. $M_\infty = 2 \cdot 30$. $Re_\infty = 2 \cdot 7 \times 10^5$ per inch. $\theta/h = 0 \cdot 008$).
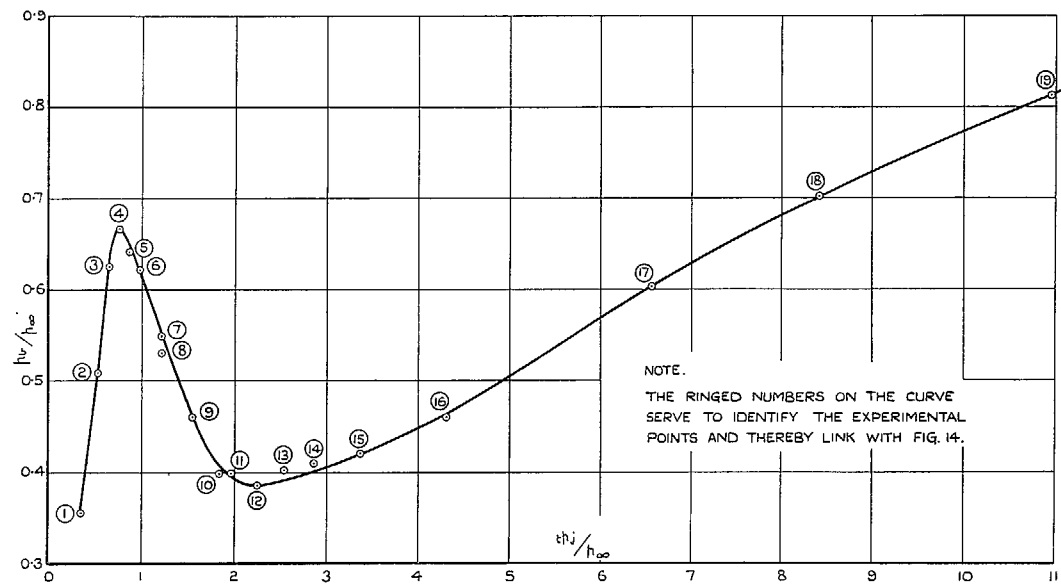
FIG. 13. Effect of internal flow on base pressure—Afterbody No. 1 $(M_\infty = 2 \cdot 30)$.

NOTE.

THE RINGED NUMBERS ON THE CURVE SERVE TO IDENTIFY THE EXPERIMENTAL POINTS AND THEREBY LINK WITH FIG. 14.
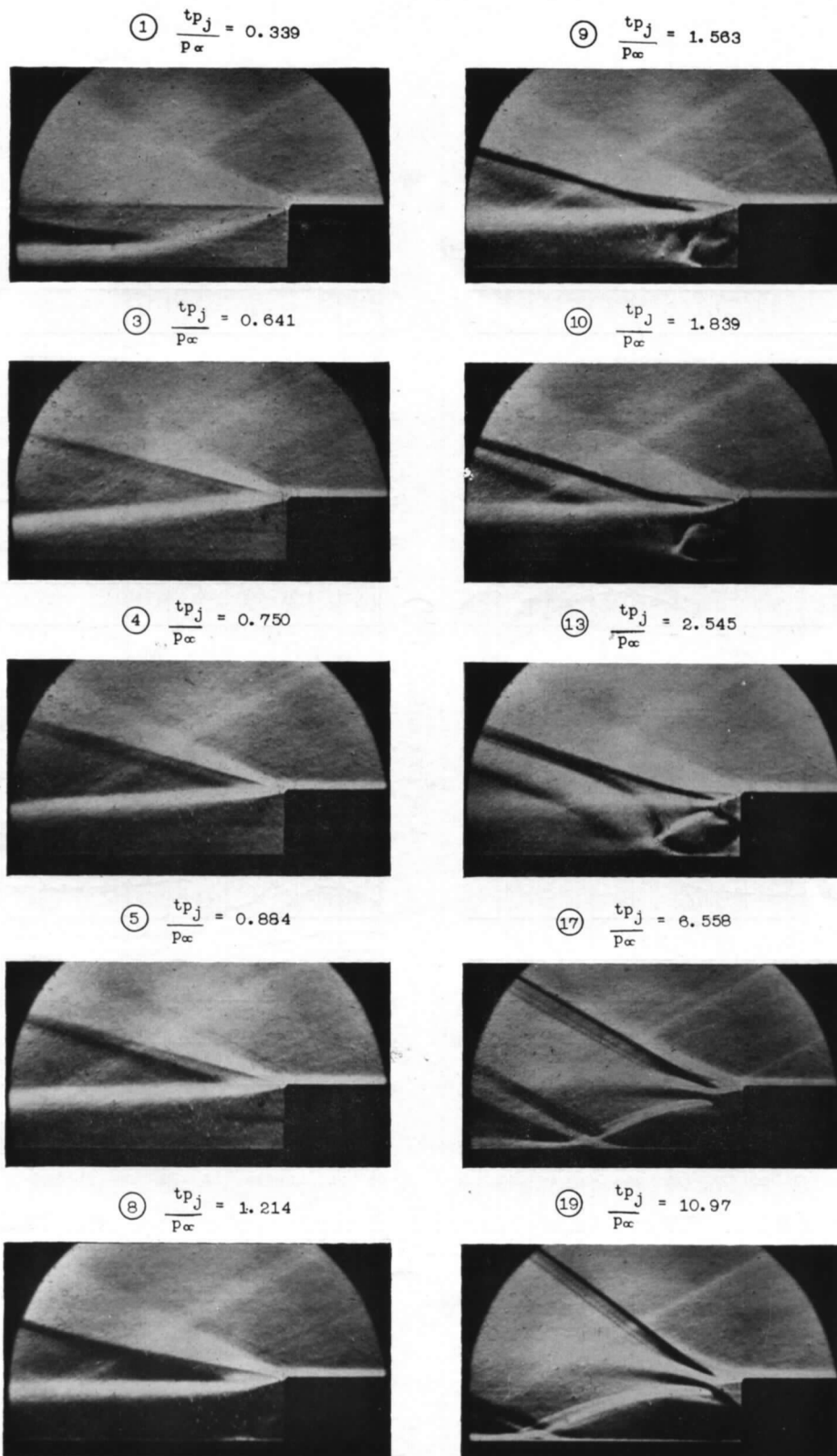
FIG. 14.   Schlieren photographs showing effect of internal jet on base flow—Afterbody No. 1
(*Note*: The ringed numbers refer to the corresponding points on the curve in Fig. 13).

25
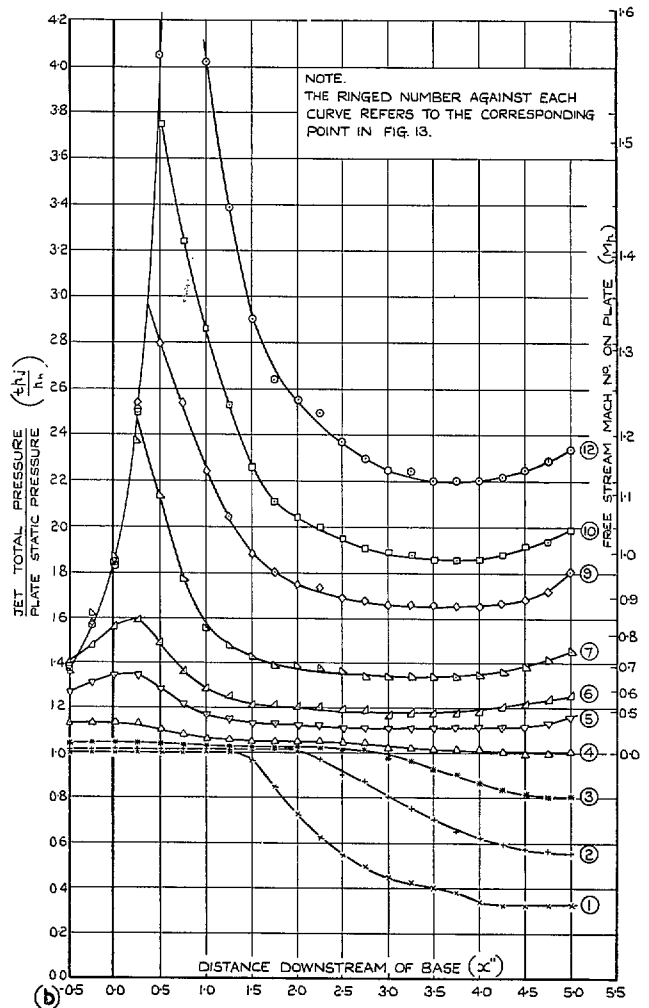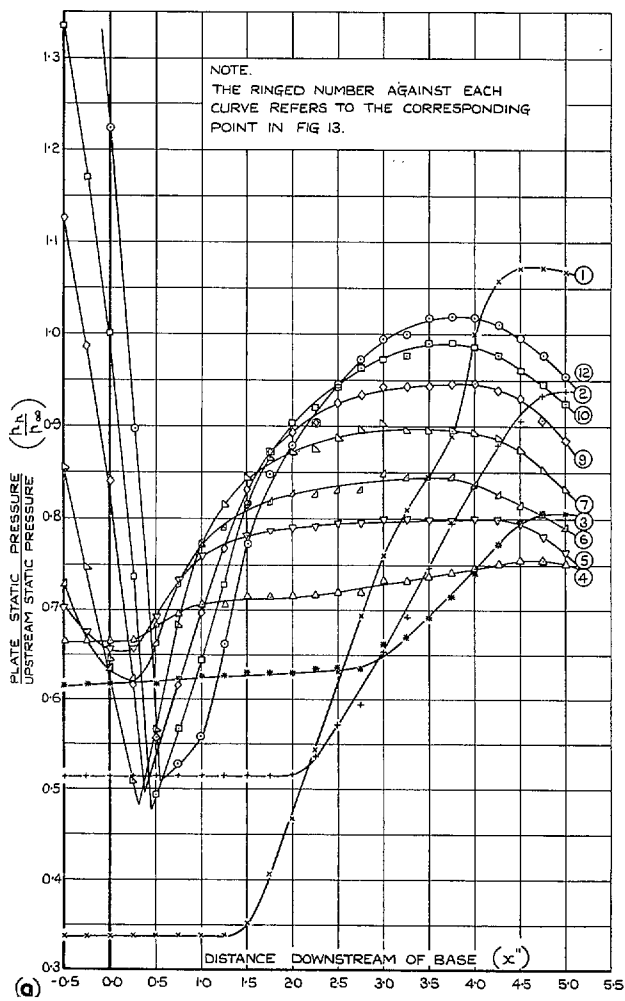
FIGS. 15a and 15b.   Effect of internal flow on Mach number and static-pressure distribution along plate—Afterbody No. 1 ($M_\infty = 2 \cdot 30$).
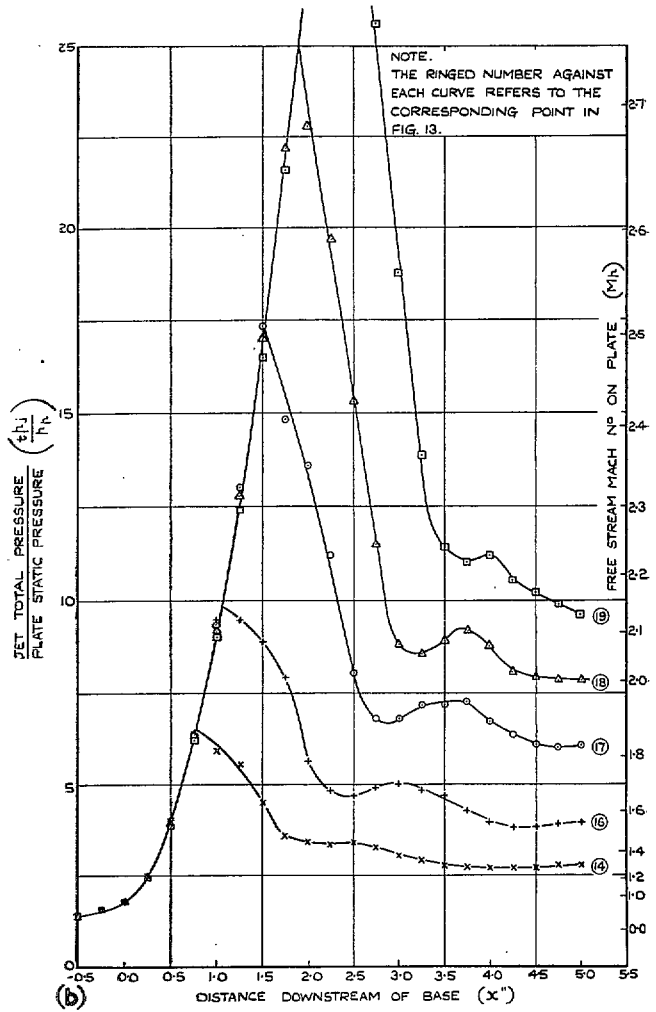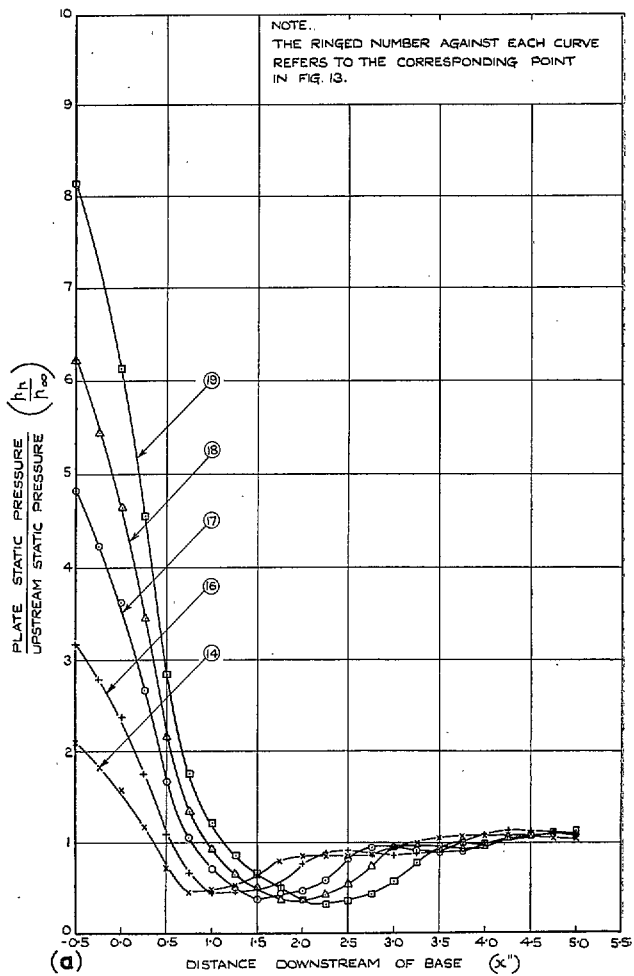
Figs. 16a and 16b. Effect of internal flow on Mach number and static-pressure distribution along plate—Afterbody No. 1 ($M_\infty = 2 \cdot 30$).

(a) FLOW PATTERN CORRESPONDING TO POINT ① IN FIG.13. NO INTERNAL FLOW.

(b) FLOW PATTERN CORRESPONDING TO POINT ② IN FIG.13. $\frac{thj}{P_{\infty}} = 0.52$.

(c) FLOW PATTERN CORRESPONDING TO POINT ④ IN FIG.13. $\frac{thj}{P_{\infty}} = 0.75$.

(d) FLOW PATTERN CORRESPONDING TO POINT ⑦ IN FIG.13. $\frac{thj}{P_{\infty}} = 1.21$.

(e) FLOW PATTERN CORRESPONDING TO POINT ⑩ IN FIG.13. $\frac{thj}{P_{\infty}} = 1.84$.

(f) FLOW PATTERN CORRESPONDING TO POINT ⑰ IN FIG.13. $\frac{thj}{P_{\infty}} = 6.56$.
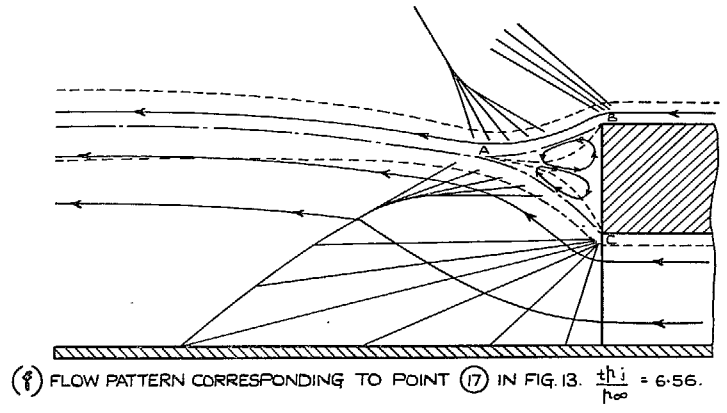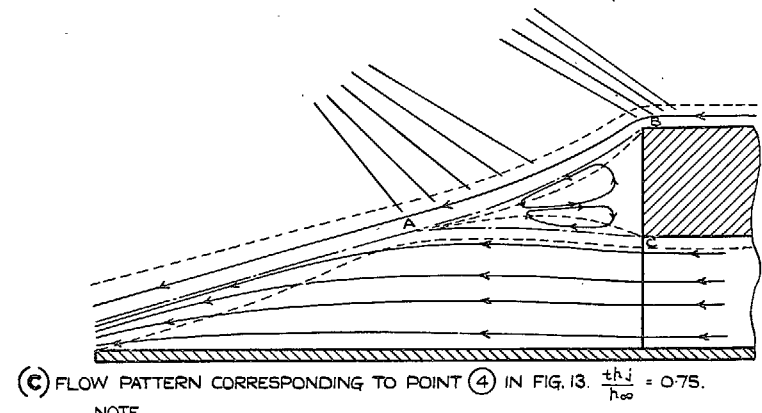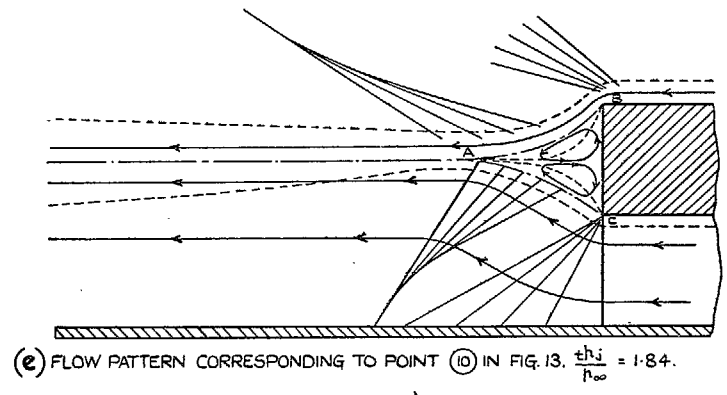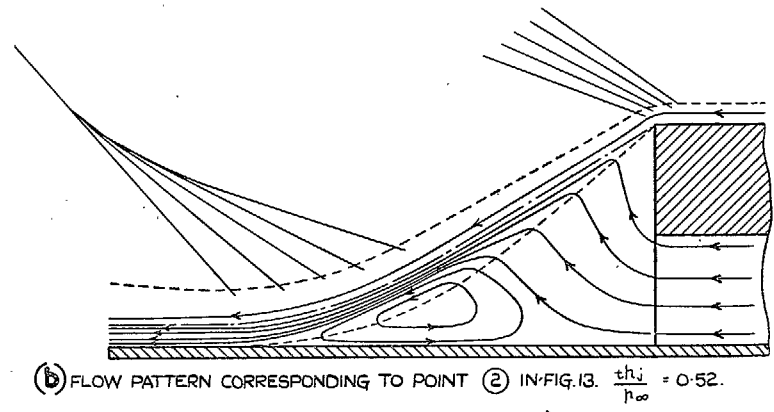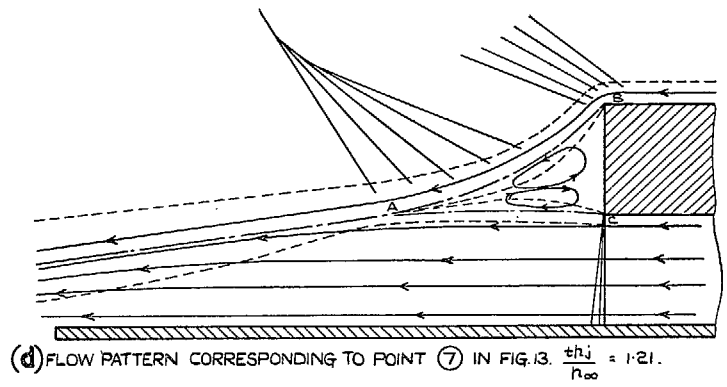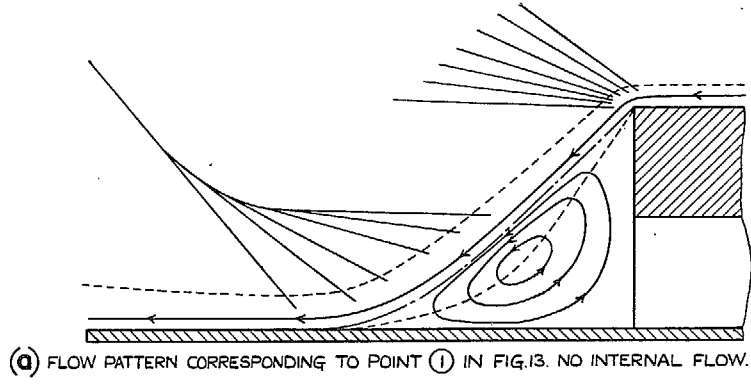
NOTE.
FLOW DIVIDING LINES SHOWN THUS ——·——   BOUNDARIES OF VISCOUS FLOW REGIONS SHOWN THUS ------   STREAMLINES SHOWN THUS ——➤——

FIGS. 17a to 17f.   Schematic diagrams showing effect of internal jet on flow pattern behind base.

28

KEY.		
AFTERBODY	BOAT TAIL ANGLE (ϵ°)	SYMBOL.
N$^\circ$. 1.	0	x
N$^\circ$. 2.	2·5	⊙
N$^\circ$. 3.	5·0	+
N$^\circ$. 4.	7·5	◇
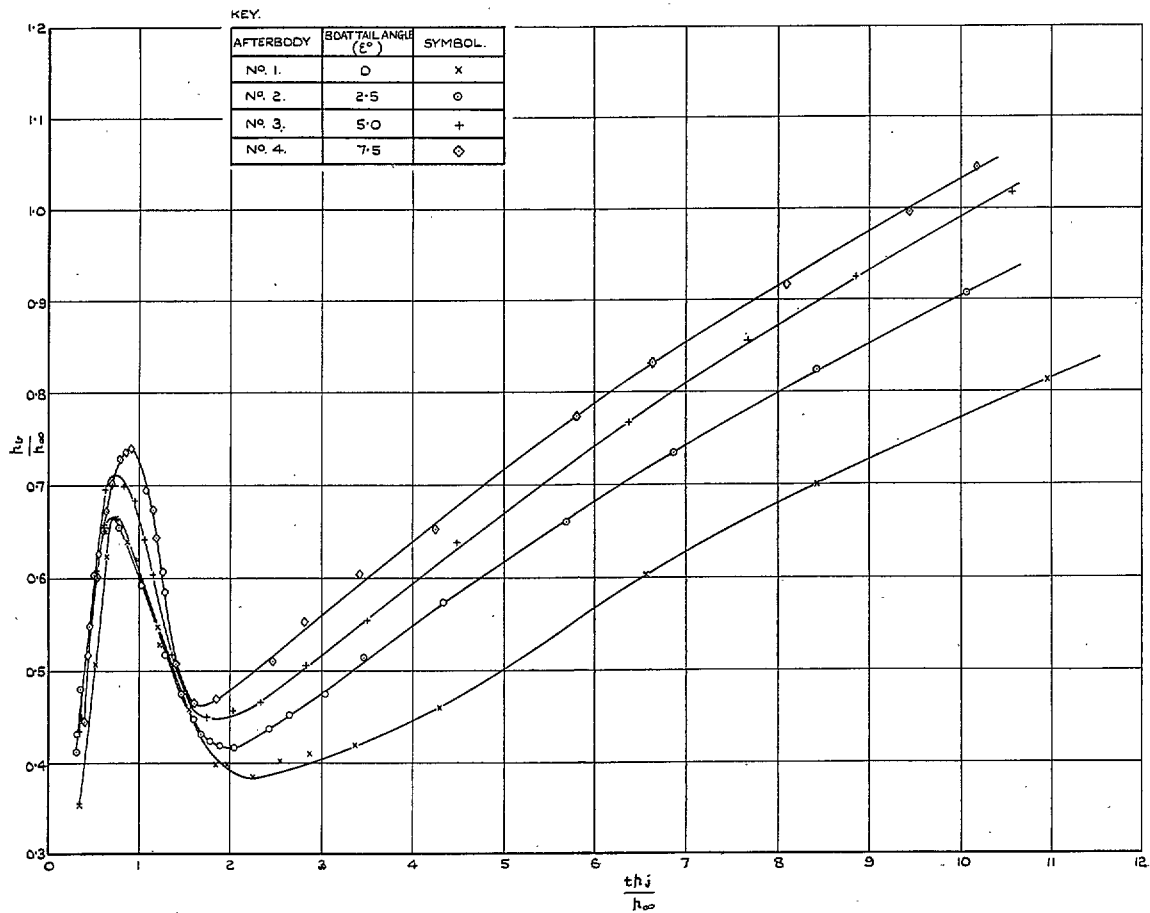
Fig. 18. Effect of internal flow on base pressure—Afterbodies Nos. 1, 2, 3 and 4 ($M_\infty = 2\cdot30$).

29
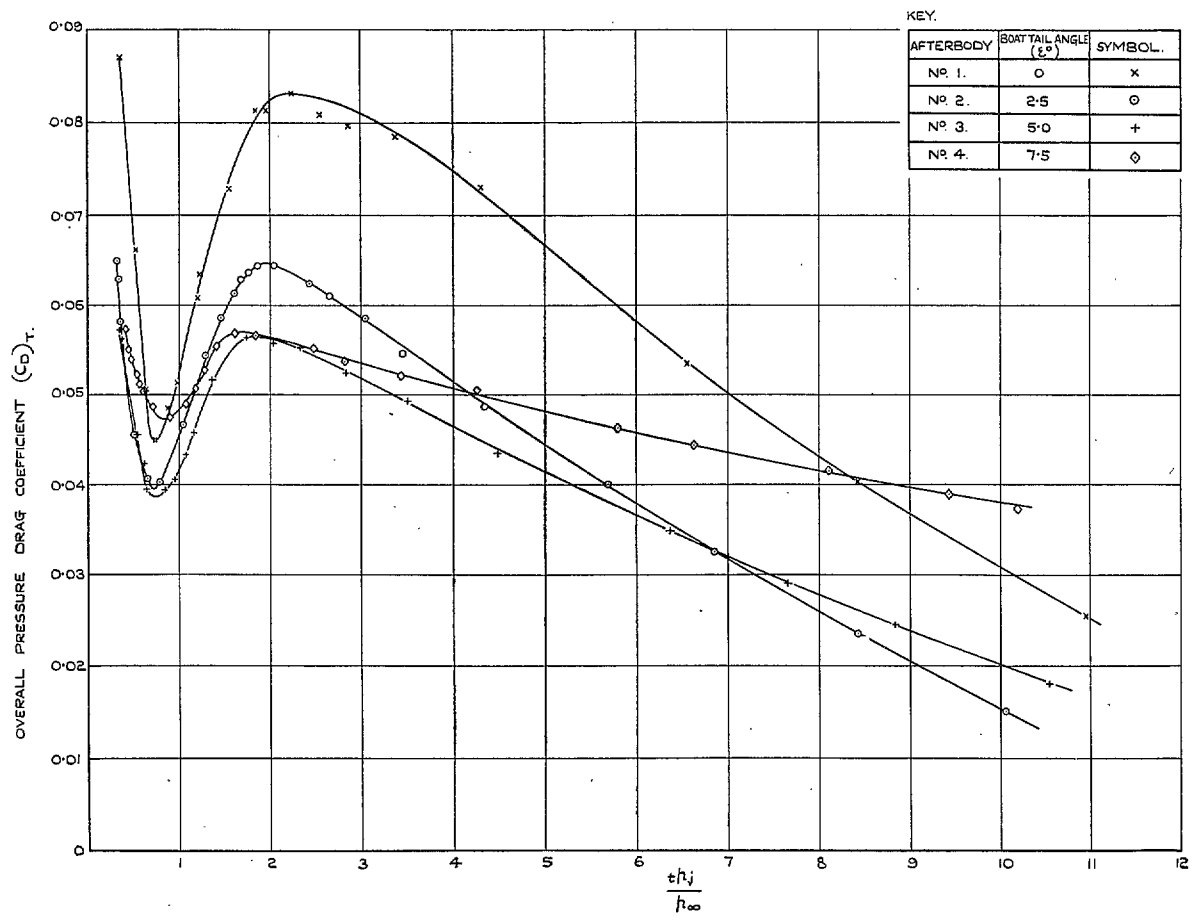
FIG. 19. Effect of internal flow on overall pressure drag coefficient—Afterbodies Nos. 1, 2, 3 and 4 $(M_\infty = 2 \cdot 30)$.
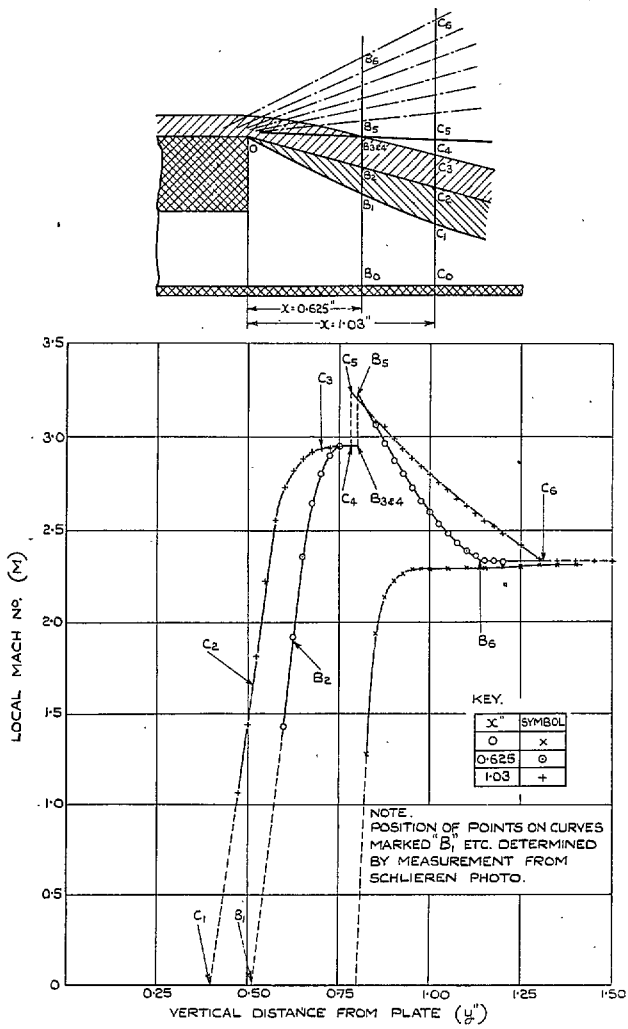
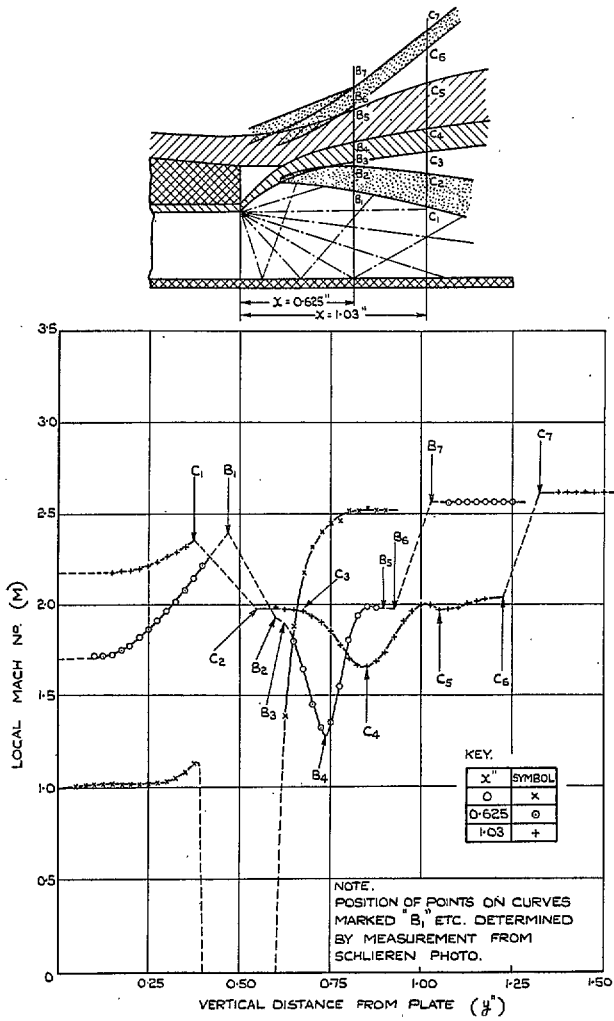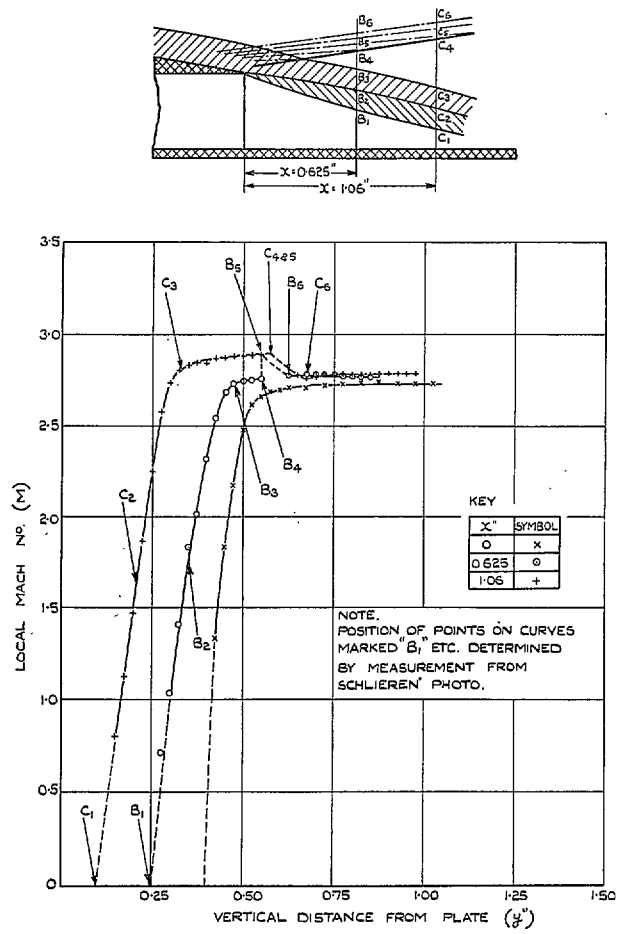FIG. 20. Mach-number distribution behind base—
Afterbody No. 1 (No internal flow).
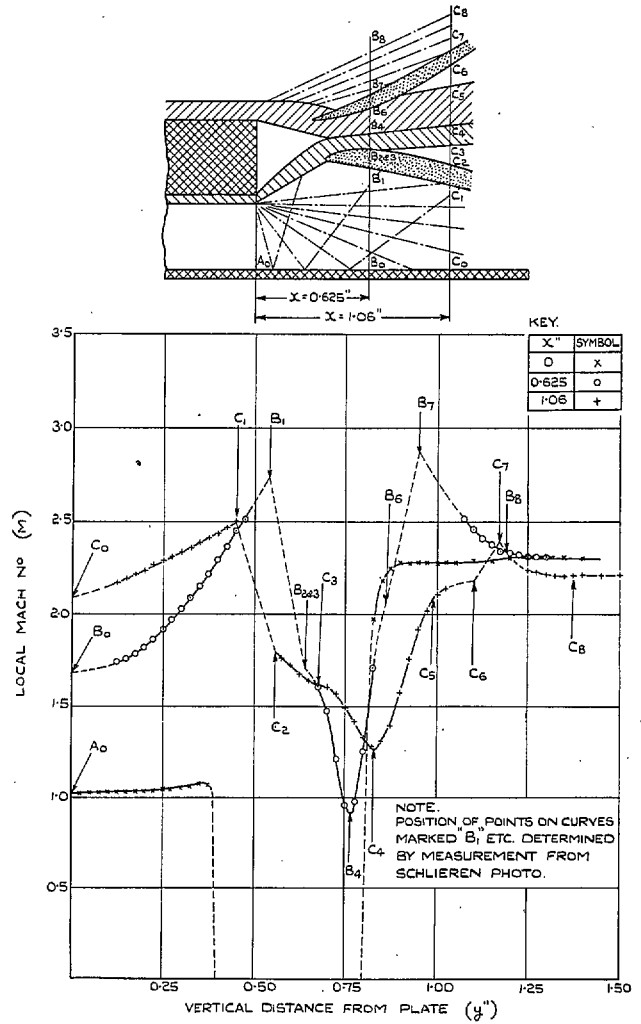
FIG. 21. Mach-number distribution behind base—
Afterbody No. 1 $({}_t p_j/p_\infty = 6 \cdot 5)$.

31
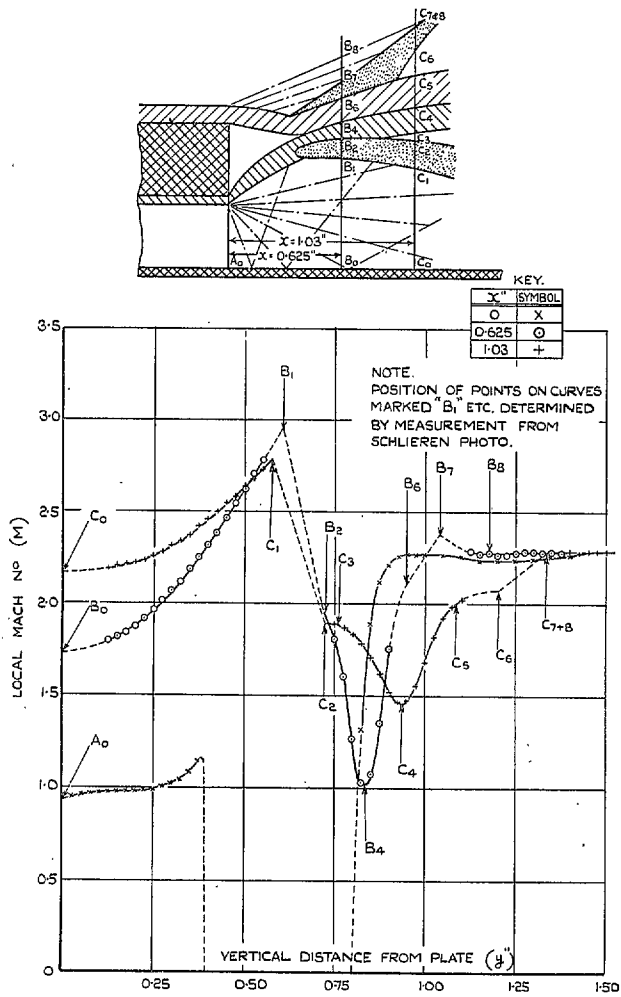
Fig. 22. Mach-number distribution behind base—
Afterbody No. 1 ($_t p_j/p_\infty = 11 \cdot 0$).
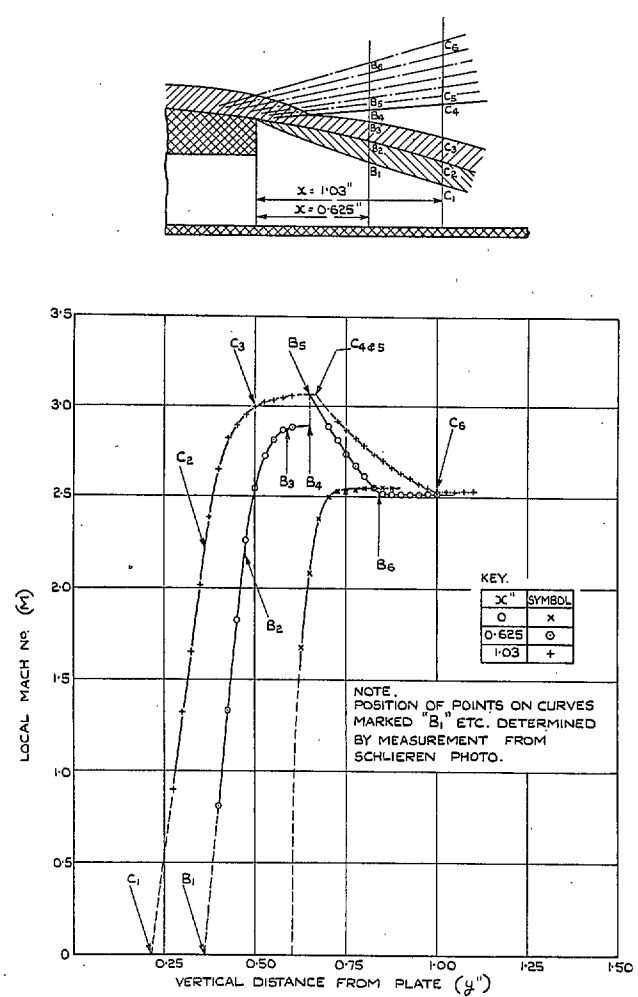
Fig. 23. Mach-number distribution behind base—
Afterbody No. 3 (No internal flow).

32

FIG. 24. Mach-number distribution behind base—
Afterbody No. 3 ($p_j/p_\infty = 11\cdot0$).

FIG. 25. Mach-number distribution behind base—
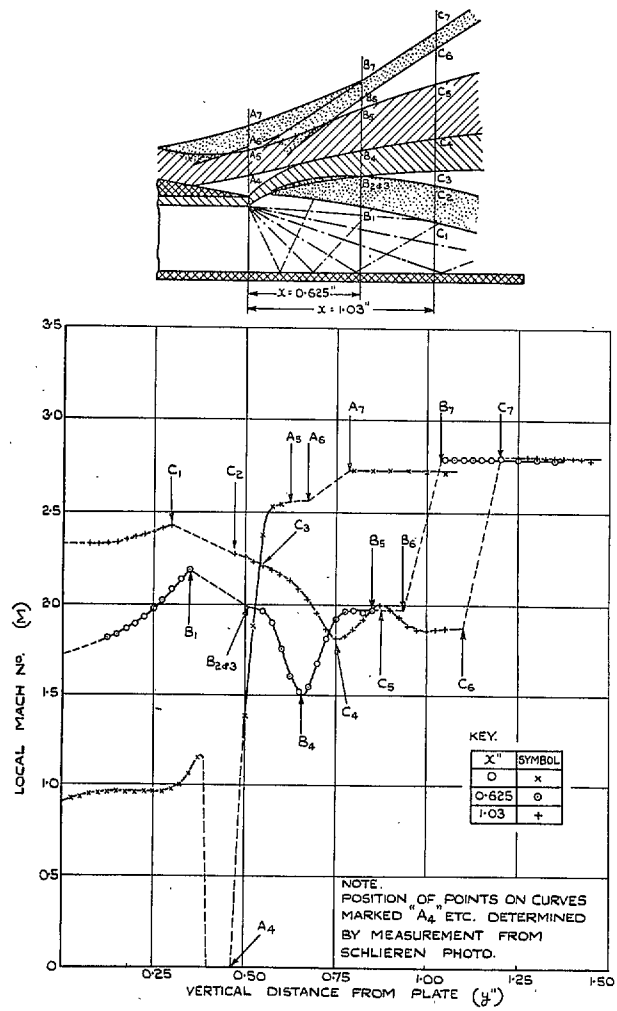Afterbody No. 5 (No internal flow).

33

FIG. 26. Mach-number distribution behind base—
Afterbody No. 5 $(_tp_j/p_\infty = 11\cdot0)$.

Publications of the Aeronautical Research Council

ANNUAL TECHNICAL REPORTS OF THE AERONAUTICAL RESEARCH COUNCIL (BOUND VOLUMES)—

1939 Vol. I. Aerodynamics General, Performance, Airscrews, Engines. 50s. (52s.)
   Vol. II. Stability and Control, Flutter and Vibration, Instruments, Structures, Seaplanes, etc. 63s. (65s.)

1940 Aero and Hydrodynamics, Aerofoils, Airscrews, Engines, Flutter, Icing, Stability and Control, Structures, and a miscellaneous section. 50s. (52s.)

1941 Aero and Hydrodynamics, Aerofoils, Airscrews, Engines, Flutter, Stability and Control, Structures. 63s. (65s.)

1942 Vol. I. Aero and Hydrodynamics, Aerofoils, Airscrews, Engines. 75s. (77s.)
   Vol. II. Noise, Parachutes, Stability and Control, Structures, Vibration, Wind Tunnels. 47s. 6d. (49s. 6d.)

1943 Vol. I. Aerodynamics, Aerofoils, Airscrews. 80s. (82s.)
   Vol. II. Engines, Flutter, Materials, Parachutes, Performance, Stability and Control, Structures. 90s. (92s. 9d.)

1944 Vol. I. Aero and Hydrodynamics, Aerofoils, Aircraft, Airscrews, Controls. 84s. (86s. 6d.)
   Vol. II. Flutter and Vibration, Materials, Miscellaneous, Navigation, Parachutes, Performance, Plates and Panels, Stability, Structures, Test Equipment, Wind Tunnels. 84s. (86s. 6d.)

1945 Vol. I. Aero and Hydrodynamics, Aerofoils. 130s. (132s. 9d.)
   Vol. II. Aircraft, Airscrews, Controls. 130s. (132s. 9d.)
   Vol. III. Flutter and Vibration, Instruments, Miscellaneous, Parachutes, Plates and Panels, Propulsion. 130s. (132s. 6d.)
   Vol. IV. Stability, Structures, Wind Tunnels, Wind Tunnel Technique. 130s. (132s. 6d.)

ANNUAL REPORTS OF THE AERONAUTICAL RESEARCH COUNCIL—

1937   2s. (2s. 2d.)   1938   1s. 6d. (1s. 8d.)   1939-48   3s. (3s. 5d.)

INDEX TO ALL REPORTS AND MEMORANDA PUBLISHED IN THE ANNUAL TECHNICAL REPORTS, AND SEPARATELY—

April, 1950 . . . . . R. & M. No. 2600   2s. 6d. (2s. 10d.)

AUTHOR INDEX TO ALL REPORTS AND MEMORANDA OF THE AERONAUTICAL RESEARCH COUNCIL—

1909-January, 1954 . . . R. & M. No. 2570   15s. (15s. 8d.)

INDEXES TO THE TECHNICAL REPORTS OF THE AERONAUTICAL RESEARCH COUNCIL—

December 1, 1936 — June 30, 1939   R. & M. No. 1850   1s. 3d. (1s. 5d.)
July 1, 1939 — June 30, 1945   R. & M. No. 1950   1s. (1s. 2d.)
July 1, 1945 — June 30, 1946   R. & M. No. 2050   1s. (1s. 2d.)
July 1, 1946 — December 31, 1946   R. & M. No. 2150   1s. 3d. (1s. 5d.)
January 1, 1947 — June 30, 1947   R. & M. No. 2250   1s. 3d. (1s. 5d.)

PUBLISHED REPORTS AND MEMORANDA OF THE AERONAUTICAL RESEARCH COUNCIL—

Between Nos. 2251-2349   R. & M. No. 2350   1s. 9d. (1s. 11d.)
Between Nos. 2351-2449   R. & M. No. 2450   2s. (2s. 2d.)
Between Nos. 2451-2549   R. & M. No. 2550   2s. 6d. (2s. 10d.)
Between Nos. 2551-2649   R. & M. No. 2650   2s. 6d. (2s. 10d.)
Between Nos. 2651-2749   R. & M. No. 2750   2s. 6d. (2s. 10d.)

Prices in brackets include postage

HER MAJESTY'S STATIONERY OFFICE